Chapter 4
Gaseous Detectors

H. J. Hilke and W. Riegler

4.1 Introduction

All gaseous detectors signal the passage of charged particles by gathering the electrons from the ion pairs produced in the gas, usually after some amplification. The history of the gas detectors starts with the counter described by Rutherford and Geiger in 1908 [1]. It consisted of a cylindrical metallic tube filled with air or other simple gases at some 5 Torr and with a 0.45 mm diameter wire along its axis. The negative high voltage on the tube with respect to the wire was adjusted to below the discharge limit. With a gas gain of a few 10^3, only α-particles could be detected as current pulses with an electrometer. This counter was the first electronic counter, following the optical counting of light flashes in the study of radioactive substances with scintillating crystals. A major step was taken when Geiger found that by replacing the anode wire by a needle with a fme pin, electrons could also be detected [2]. These *needle counters* became the main particle counter for years. Already in 1924, Greinacher started using electronic tubes to amplify the signals [3].

The *Geiger-Mueller-counter* was first described in 1928 [4]: it produced strong signals independent of the primary ionization. Used with rare gases, these counters required load resistances of $10^8 - 10^9$ Ohm to avoid continuous discharges, resulting in dead times of $10^{-3} - 10^{-4}$ s. Later, external circuits were introduced to shorten the dead time. The real progress, however, brought the discovery in 1935 by Trost [5] that the addition of alcohol quenches the gas discharges internally,

The author H. J. Hilke is deceased at the time of publication.

H. J. Hilke · W. Riegler (✉)
CERN, Geneva, Switzerland
e-mail: Werner.Riegler@cern.ch

C. W. Fabjan, H. Schopper (eds.), *Particle Physics Reference Library*,
https://doi.org/10.1007/978-3-030-35318-6_4

permitting low load resistances and thus high counting rates. Cosmic ray physics in particular profited from systems of such counters used with electron tube coincidence circuits. It took a number of years to understand the basic processes in different gases and under various operation conditions.

Proportional counters regained interest, when the development of more sensitive readout electronics permitted energy determination. In the second half of the 1940s, however, the demand for faster counters with longer lifetime and higher sensitivity initiated a move towards scintillation techniques, which saw a rapid development, especially after the introduction of the photomultiplier, soon providing fast response and time resolutions below 10^{-8} s. On the gas detector side, only the novel technique *of parallel plate counters* [6] could compete, with time resolutions down to 10^{-10} s, however with lower rate capability. A detailed account of the developments up to the 1950s can be found in [7].

The field of gas detectors was revived with the introduction of the *multiwire proportional chamber* by Charpak in 1968 [8] and shortly afterwards with the extension by two groups to *drift chambers* with different geometries [9, 10]. The following decades saw a rapid development of the techniques, especially in high energy physics but also for nuclear physics and other fields. An additional major R&D effort was triggered in the 1990s by the requirements for the LHC: extreme particle rates and radiation hardness. Solutions demanded very careful choice of gas fillings as well as of construction materials and methods. Gas detectors were and are still used mainly for tracking but also in calorimeters, Cherenkov counters and the detection of transition radiation. Only in the layers closest to the interaction points in accelerator experiments and in other applications where spatial resolution is the prime requirement, finely grained silicon detectors have taken over as first choice. Most of the detector developments were made possible only by the extremely rapid progress in the field of electronics, with respect to miniaturization, integration density, cost and radiation hardness.

Powerful simulation programs have been developed in the past decades and have been widely used in the development and optimization of gas detectors. The program *Garfield* [11] calculates electric fields, electron and ion trajectories and induced signals. The program *Heed* [12] describes primary ionization produced by fast particles in gases and the program *Magboltz* [13] electron transport properties in gas mixtures. The agreement of simulation and measurement has become impressive.

We shall at several occasions refer to designs and studies from the LHC experiments. Recent detailed reports them may be found in [14–17]. The development of the last years can well be followed in the Proceedings of the Vienna Conference on Instrumentation initiated in 1977 as Wire Chamber Conference on a tri-annual basis [18] and of the annual IEEE Nuclear Science Symposia.

The following sections will start with a description of the basic processes in gaseous detectors: ionization of the gas by charged particles (Sect. 4.2.1), transport of electrons and ions in electric and magnetic fields (Sect. 4.2.2), avalanche amplification in high electric fields (Sect. 4.2.3), formation of the readout signals (Sect. 4.2.4) and ‘ageing’ of detectors under irradiation (Sect. 4.2.6). A discussion

of major directions of detector design and performance follows in Sect. 4.3: Single-wire tubes (Sect. 4.3.1), Multi-Wire-Proportional Chambers (Sect. 4.3.2), Drift Chambers (Sect. 4.3.3), Resistive Plate Chambers (Sect. 4.3.4) and Micropattern Devices (Sect. 4.3.5).

4.2 Basic Processes

As most processes depend on the velocity of a particle, we shall often state numerical values for minimum ionizing particles (*mip*), i.e. for $\gamma = 3 - 4$.

4.2.1 Gas Ionization by Charged Particles

The passage of charged particles through a gas is signaled by the production of electron/ion pairs along its path. The electrons are attracted by electrodes on positive potential, in the vicinity of which they are usually amplified in a avalanche process. We give a short summary of the various aspects of the ionization processes, following to some extent [19].

4.2.1.1 Primary Clusters

The ionizing collisions of the particle are occurring randomly with a *mean distance* λ, related to the ionization cross-section per electron σ_{I} and the electron density N_{e} of the gas:

$$1/\lambda = N_{\mathrm{e}}\, \sigma_{\mathrm{I}}. \tag{4.1}$$

The number k of ionizing collisions on a path length L thus follows a Poisson distribution with mean L/λ:

$$\mathrm{P}\,(k|L,\ \ \lambda) = \left((L/\lambda)^k/k!\right) \exp\left(-L/\lambda\right). \tag{4.2}$$

The probability to have no ionization in L is

$$\mathrm{P}\,(0|L,\ \ \lambda) = \exp\left(-L/\lambda\right). \tag{4.3}$$

This relation is used to determine λ and defines the *inefficiency* of a counter measuring a track length L, if it is sensitive to a single primary electron.

The probability distribution f(l)dl for a free flight pass l between two ionizing collisions—i.e. the probability of no ionization in l and one in dl-is an exponential,

$$\mathrm{f}(l)\mathrm{d}l = (\mathrm{d}l/\lambda)\exp(-l/\lambda), \tag{4.4}$$

i.e. short distances are favoured.

An electron ejected in a primary collision on atom A may have enough energy to ionize one or more other atoms. Thus *clusters* of two or more electrons are formed by *secondary ionization*. These clusters are mostly rather localized, as the ejection energy is usually low and results in a short range. High ejection energies for so-called *δ-electrons* are rare, their average number per cm is approximately inversely proportional to energy:

$$P(E > E_0) - y/\left(\beta^2 \mathrm{E}_0\right)/\mathrm{cm}, \tag{4.5}$$

with E_0 in keV, and $y = 0.114$ for Ar, and $y = 0.064$ for Ne [20]; β= particle velocity/speed of light in vacuum. Thus, in Ar, for β~1 and $E_0 = 10\,\mathrm{keV}$, $P = 0.011$/cm, i.e., on average one collision with $E > 10\,\mathrm{keV}$ will occur on a track length of 90 cm. The range of a 10 keV electron is about 1.4 mm. The range decreases very rapidly with decreasing energy and is only about 30 μm for a 1 keV electron.

It tums out that, although the majority of the 'clusters' consist of a single electron, clusters of size >1 contribute significantly to the *mean total number n_T of electrons produced per cm*, so that n_T is significantly larger than n_p, the *mean number of primary clusters per cm*. Table 4.1 gives experimental values for some of the common detector gases. In Ar at NTP one finds on average $n_\mathrm{p} = 26$ and $n_\mathrm{T} = 100$ electrons/cm for a minimum ionizing particle, where n_T depends on the volume around the track taken into account. The most probable value for the total ionization is $n_\mathrm{mp} = 42$ electrons/cm. The big difference between n_T and n_mp is an indication of the long tail of the distribution.

Table 4.1 Properties of gases at 20°C, 1 atm

Gas	n_p	n_T	w [eV]	E_I [eV]	E_x [eV]	p [mg/cm^3]
He	4.8	7.8	45	24.5	19.8	0.166
Ne	13	50	30	21.6	16.7	0.84
Ar	25	100	26	15.7	11.6	1.66
Xe	41	312	22	12.1	8.4	5.50
CH_4	37	54	30	12.6	8.8	0.67
CO_2	35	100	34	13.8	7.0	1.84
i-butane	90	220	26	10.6	6.5	2.49
CF_4	63	120	54	16.0	10.0	3.78

n_p, n_T mean primary and total number of electron-ion pairs per cm; w: average energy dissipated per ion pair; E_I, E_x: lowest ionization and excitation energy [21]

4.2.1.2 Cluster Size Distribution

The space resolution in gaseous detectors is influenced not only by the Poisson distribution of the primary clusters along the track but also by the *cluster size distribution*, i.e., by the number of electrons in each cluster and their spatial extent. Little was known experimentally (except for some measurements in cloud chambers) until the first detailed theoretical study [22] for Ar at 1 atm and 20°C. Based on the experimental cross-sections for photo absorption, the oscillator strengths and the complex dielectric constants are calculated and from this the distribution of energy transfers larger than the ionization energy (15.7 eV). Finally, a detailed list is obtained for the distribution of cluster sizes for $\gamma = 4$ and $\gamma = 1000$, to estimate the relativistic rise. A cut of 15 keV was applied to the maximum energy transfer, thus concentrating on the local energy deposition. The mean number of clusters is found to be $n_p = 26.6$/cm at $\gamma = 4$, and 35/cm at $\gamma = 1000$. For a MIP, 80.2% of the clusters are found to contain 1 electron, 7.7% two electrons, 2% three electrons, and 1.4% more than 20 electrons.

Several years later, a detailed experimental study of several gases is reported in [23]. For Ar, 66/15/6 and 1.1% of the clusters are found to contain 1/2/3 and $\geq$20 electrons, respectively. The values for low cluster sizes are quite different from the calculated values mentioned above and the calculated bump around 10 electrons is not seen in the measurement, see Fig. 4.1. The authors suggest as a possible explanation that one assumption made in the simulation may not be appropriate, namely that the absorption of virtual photons can be treated like that of real photons, which also leads to the bump at the L-absorption edge. A simpler model starting from measured spectra of electrons ejected in ionizing collisions gives good agreement with the measurements, in particular for the probability of small cluster sizes.

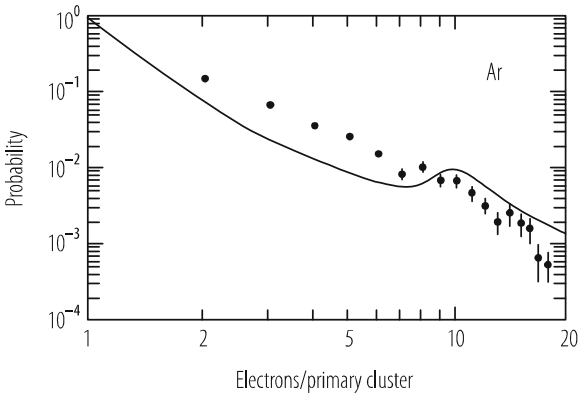

Fig. 4.1 Cluster size distribution: simulation for Ar (continuous line) [22] and measurements in Ar/CH_4 (90/10%) [23]

Space resolution in drift chambers is influenced by the clustering in several ways. The arrival time of the first n electrons, where n times gas amplification is the threshold for the electronics, depends both on the spatial distribution of the clusters and the cluster size. For large clusters, δ-electrons, ionization may extend far off the trajectory.

4.2.1.3 Total Number of Ion Pairs

The detector response is related to the cluster statistics but also to the total ionization n_T, e.g., in energy measurements. A quantity W has been introduced to denote the average energy lost by the ionizing particle for the creation of one ion pair:

$$W = E_i/n_E, \tag{4.6}$$

where E_i is the initial kinetic energy and n_E the average total number of ion pairs *after full dissipation of* E_j.

Measurements of W by total absorption of low energy particles show that it is practically independent of energy above a few keV for electrons and above a few MeV for α-particles. For that reason the differential value w, defined by

$$w = x < \mathrm{d}E/\mathrm{d}x > / < n_T > \tag{4.7}$$

may be used alternatively, as is usually done in Particle Physics, to relate the average total number of ion pairs n_T, created in the track segment of length x, to the average energy lost by the ionizing particle. For relativistic particles, $\mathrm{d}E/\mathrm{d}x$ can not be obtained directly from the difference of initial and final energy (about 270 keV/m for $\gamma = 4$ in Ar), as it is below the measurement resolution. Therefore, w has to be extrapolated from measurements of lower energy particles. For the rare gases one finds $w/I = 1.7 - 1.8$ and for common molecular gases $w/I = 2.1 - 2.5$, where I is the *ionization potential*, indicating the significant fraction of $\mathrm{d}E/\mathrm{d}x$ spent on excitation. Values for photons and electrons are the same, also for α particles in rare gases; in some organic vapours they may be up to 15% higher for α-particles. At low energy, close to the ionization potential, W increases.

In gas mixtures, where an excitation level of component A is higher than I of component B, excited molecules of A often produce a substantial increase in ionization, as has e.g. been observed even with minute impurities in He and Ne: adding 0.13% of Ar to He changed W from 41.3 to 29.7 eV per ion pair. This energy transfer is called *Jesse effect* or *Penning effect*, if metastable states are involved. It is also possible that more than one electron is ejected from a single atom, e.g., by Auger effect following inner shell ionization.

The distribution of n_T in small gas segments is very broad, see an example in Fig. 4.2 [24]. To describe the measurement result, it is thus appropriate to use the *most probable value* instead of the *mean*, since the mean of a small number of measurements will depend strongly on some events from the long tail

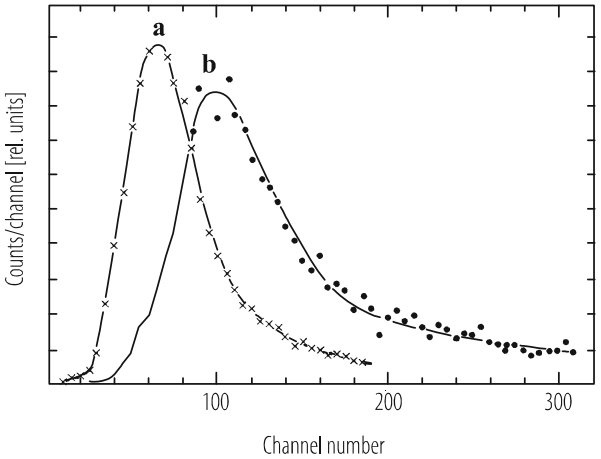

Fig. 4.2 Measured pulse height distribution for 2.3 cm in Ar/CH_4 at 1 atm: (**a**) protons 3 GeV/c, (**b**) electrons 2 GeV/c [24]

of the distribution. The measured pulse height spectrum contains some additional broadening from the fluctuations of the avalanche process. For a mixture of Ar and 5% CH_4, a most probable value of $n_{\mathrm{mp}} = 48$ ion pairs/cm was found for minimum ionizing particles [25].

4.2.1.4 Dependence of Energy Deposit on Particle Velocity

As mentioned above, for position detectors one is interested in the ionization deposited close to the particle trajectory. The Bethe-Bloch formula for dE/dx describes instead the average total energy loss from the incoming particle, including the energy spent on the ejection of energetic δ-electrons which deposit ionization far from the trajectory. To describe the local energy deposit, it is sensible to exclude the contribution from these energetic δ-electrons. This is done by replacing the maximum possible energy transfer T_{max} by a cut-off energy $T_{\mathrm{cut}} << T_{\mathrm{max}}$. This energy cut-off will depend on the experimental conditions and may lie between 30 keV and 1 MeV (in a magnetic field) [19] One then obtains the modified Bethe-Bloch formula for the *mean restricted energy deposit* [20, 21] (see also Chap. 2)

$$\mathrm{d}E/\mathrm{d}x_{\mathrm{restricted}} = K z^2 \, (Z/A) \left(1/\beta^2\right) \left[0.5 \ln \left(2 m_{\mathrm{e}} c^2 \beta^2 \gamma^2 T_{\mathrm{cut}} / I^2\right) - \beta^2/2 - \delta/2\right], \tag{4.8}$$

with $K = 4\pi N_{\mathrm{A}} r_{\mathrm{e}}^2 m_{\mathrm{e}} c^2$, N_{A} = Avogadro constant, m_{e}, r_{e}= mass and classical radius of the electron.

Due to the cut-off, this relation applies not only to heavy particles but also to ionization by electrons [19]. The minimum dE/dx deposited by a *minimum ionizing particle* (mip) still lies around $\gamma = 3 - 4$, with $\delta = 0$. For $\beta \to 1$, the *density correction* δ approaches

$$\delta \to 2 \ln \left(h v_{\mathrm{p}} \gamma / I \right) - 1, \tag{4.9}$$

hv_{p} being the quantum energy of the plasma oscillation of the medium. The restricted energy deposit then reaches a constant value, the *Fermiplateau*, the δ-term compensating the $\ln\gamma$ term:

$$\mathrm{d}E/\mathrm{d}x_{\mathrm{restricted}} \to \mathrm{P}^2 \, (Z/A) \, 0.5 \ln \left[2mc^2 T_{\mathrm{cut}} / \left(h v_{\mathrm{p}} \right)^2 \right]. \tag{4.10}$$

In Ar one obtains for the ratio R of energy deposit on the Fermi plateau to the minimum deposit $R = 1.60$, 1.54, and 1.48 for a cut-off $T_{\mathrm{cut}} = 30$,150 and 1000 keV, respectively [19]. A precise determination of R requires a good estimate of T_{cut}.

To use the β-dependence of dE/dx for particle identification, one has to measure many samples and take their *truncated mean*, e.g., the mean of the lowest 50% pulse heights, to be insensitive to the long tail and to obtain an approximation to the most probable value. See Chap. 2 for details.

4.2.2 Transport of Electrons and Ions

4.2.2.1 Drift Velocities

On the microscopic scale, electrons or ions drifting through a gas are scattered on the gas molecules. In a homogenous electric field E they will acquire a constant *drift velocity* u in the E field direction or, in the presence of an additional magnetic field B, in a direction determined by both fields. Their drift velocities are much smaller than their *instantaneous velocities* c between collisions. Electrons and ions will behave quite differently because of their mass difference.

In the chapters on drift velocities and diffusion we shall follow the argumentation developed in [19]. A relatively simple derivation brings out the main characteristics and does describe a number of experimental results with good approximation. The main approximation of the simple models is to take a single velocity c to represent the motion between collisions. In reality, these velocities c are distributed around a mean value. The shape of the distribution depends on the variation of cross-section and energy loss with the collision velocity. The rigorous theory takes these distributions into account. For lowest velocities there is only elastic scattering, for higher energies various inelastic processes contribute. The elastic and the inelastic spectrum may be described by a single *effective cross-section* $\sigma(c)$ combining the various processes, sometimes called *momentum transfer cross-section*, and by the *average fractional energy loss* $\Delta(c)$ per collision.

Collision cross-sections σ have in some cases been measured directly. Often, however, σ as well as $\Delta(c)$ have to be deduced from measurements of $u(E)$, the dependence of on E, and of diffusion, based on some assumptions on the excitation functions. The consistency of the methods, when applied to other gas mixtures, has improved over the years and is presently very good in a number of practical cases, in particular for the Magboltz simulation [13]; for a comparison of experiments with various models see e.g. [26].

Drift of Electrons

Because of their small mass, electrons will scatter isotropically in a collision and forget any preferential direction. They will acquire a *drift velocity* u given by the product of the acceleration eE/m and the average time τ between collisions

$$u = eE\tau/m. \tag{4.11}$$

Instead of, the notion of *mobility* μ is often used, with μ defined by

$$u = \mu E \rightarrow \mu = e\tau/m. \tag{4.12}$$

Over a drift distance x there will be a balance between the *collision loss* $\Delta\varepsilon_E$ and the energy picked up:

$$(x/u)\,(1/\tau)\,\Delta\varepsilon_E = eEx. \tag{4.13}$$

Here ε_E is the energy gained between collisions, Δ the average fraction of the energy lost in a collision, and $(x/u)(1/\tau)$ the number of collisions on a distance x.

For an *instantaneous velocity* c, the mean time τ between collisions is related to the collision cross- section σ and the number density N of gas molecules by

$$1/\tau = N\sigma c. \tag{4.14}$$

The total energy ε of the electron is given by

$$(m/2)\,c^2 = \epsilon = \epsilon_E + (3/2)\,kT, \tag{4.15}$$

including the thermal energy.

In the approximation $e >> (3/2)kT$, which is often fulfilled for drift of electrons in particle detectors, one obtains

$$\begin{aligned} u^2 &= (eE/mN\sigma)\,\sqrt{(\Delta/2)}\,, \text{ and} \\ c^2 &= (eE/mN\sigma)\,\sqrt{(2/\Delta)} \quad \text{for } \varepsilon - \varepsilon_E >> (3/2)\,kT. \end{aligned} \tag{4.16}$$

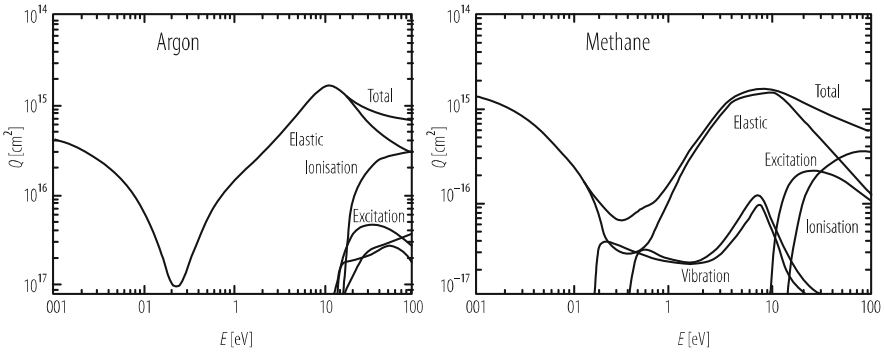

Fig. 4.3 Electron collision cross-sections for Argon and Methane used in Magboltz [13, 27]

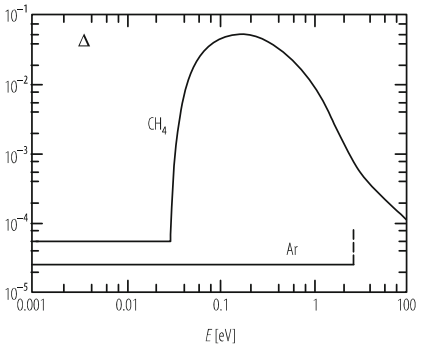

Fig. 4.4 The fraction Δ of energy lost per collision as function of mean energy ε of the electron [28]

The rigorous theory assuming a Dryvestem distribution for the random velocities c adds a multiplication factor of 0.85 to the right sides.

It is important to note that E and N only appear as E/N, the reduced electric field, for which often a special unit is used: one *Townsend* (*Td*) with 1 Td $=10^{-17}$ Vcm^2.

The important role of σ and Δ is obvious; both depend on ε. Below the first excitation level the scattering is elastic and $\Delta - 2m/M - 10^{-4}$ for electrons scattered on gas molecules with mass M. For a high drift speed a small σ is required. Figure 4.3 shows the cross-sections σ for Ar and CH_4. A pronounced minimum, the so-called 'Ramsauer dip' is clearly visible. It leads to high drift velocities in Ar - CH_4 mixtures at low E-values. TPCs take advantage of this.

10^{-17} Vcm^2 =250 V/cm atm at 20°C.

From precise measurements of drift velocity u (to 1%) and longitudinal diffusion D/μ (to 3–5%), σ and Δ have been deduced for some gases [28]. The consistency of the calculated values with measurements of u and D/μ in various other gas *mixtures* gives confidence in the method. Figure 4.4 presents calculated values for Δ as function of ε. Figure 4.5 shows $\varepsilon_k = (2/3)\varepsilon$ derived in the same way in another

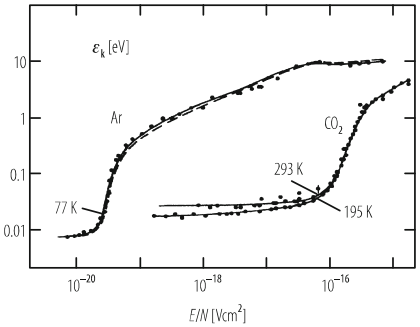

Fig. 4.5 Values for the electron energy ε derived from diffusion measurements as function of the reduced electrical field [29]

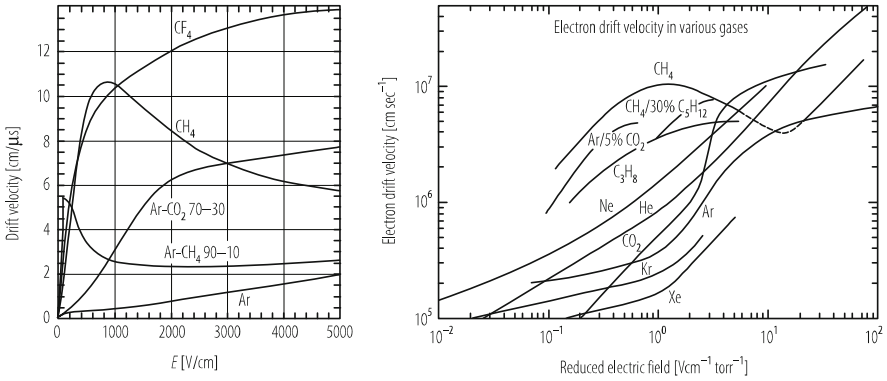

Fig. 4.6 Some examples measured electron drift velocities. (*left*) [30], (*rights*) [31]

study for two extremes, *cold* CO_2 and *hot* Ar [29]. Gases are denoted as *cold*, if ε stays close to the thermal energy $(3/2)kT$ in the fields under consideration. This is the case for gases with vibrational and rotational energy levels, the excitation of which causes inelastic energy losses to the drifting electrons. Cold gases are of interest since they exhibit the smallest possible diffusion.

For *gas mixtures* with number densities $n_i (N = \Sigma\, n_i)$, the effective σ and Δ are given by

$$\sigma = \Sigma n_i \sigma_1 / N, \text{ and}$$

$$\Delta\sigma = \Sigma n_i \Delta_i \sigma_1 / N. \tag{4.17}$$

At low E, drift velocities rise with electric field. Some (e.g. CH_4 and Ar Ar - CH_4 mixtures) go through a maximum, decrease and may rise again. Drift velocities are shown in Fig. 4.6 for some gases [30, 31].

Drift of Ions

Ions of mass m_i acquire the same amount of energy between two collisions as electrons but they lose a large fraction of it in the next collision and their random energy thus remains close to thermal energy. On the other hand the direction of their motion is largely maintained. The result is a much smaller diffusion compared to electrons and constant mobility up to high fields (to ~20 kV/cm atm for A^+ ions in A). In the *approximation for low E field*, the random velocity is considered thermal, i.e. the relative velocity c_rel between the ion and the gas molecules of mass M, which determines τ, is

$$c_\mathrm{rel}^2 = c_\mathrm{ion}^2 + c_\mathrm{gas}^2 = 3kT\left(m_\mathrm{i}^{-1} + M^{-1}\right) \tag{4.18}$$

An argumentation similar to the one followed for electrons [19] leads to

$$u = \left(m_\mathrm{i}^{-1} + M^{-1}\right)^{1/2} (1/3kT)^{1/2} eE/\left(N\sigma\right) \tag{4.19}$$

The ion drift velocity at *low fields* is thus proportional to the electric field. Typical values at 1 atm are around $u = 4$ m/s for $E = 200$ V/cm, to be compared with a thermal velocity around 500 m/s.

In the other extreme of *very high fields*, where thermal motion can be neglected, one finds the drift velocity being proportional to the square root of E. Measurements on noble gas ions [32] in their own gas clearly show both limits with a transition between them at about $15 - 50$ kV/cm atm; see Fig. 4.7. As typical drift fields in drift chambers are a few hundred V/(cm atm), the 'low field approximation' is usually applicable, except in the amplification region.

In a *gas mixture* it is expected that the component with the lowest ionization energy will rapidly become the drifting ion, independently of which atom was ionized in the first place. The charge transfer cross-section is in fact of similar magnitude as the other ion molecule scattering cross-sections. Even impurities rather low concentration might thus participate in the ion migration.

Magnetic Field Effects

A simple macroscopic argumentation introduced by Langevin produces results which are a good approximation in many practical cases.

The motion of a charged particle is described by

$$m\mathrm{d}\mathbf{u}/\mathrm{d}t = e\mathbf{E} + e\left[\mathbf{u}\ \mathrm{x}\ \mathbf{B}\right] - k\ \mathbf{u}, \tag{4.20}$$

where m, e and $\mathbf{u}$ are the particle's mass, charge and velocity vector, respectively; $\mathbf{E}$ and $\mathbf{B}$ are the electric and magnetic field vectors; k describes a frictional force proportional to $-\mathbf{u}$.

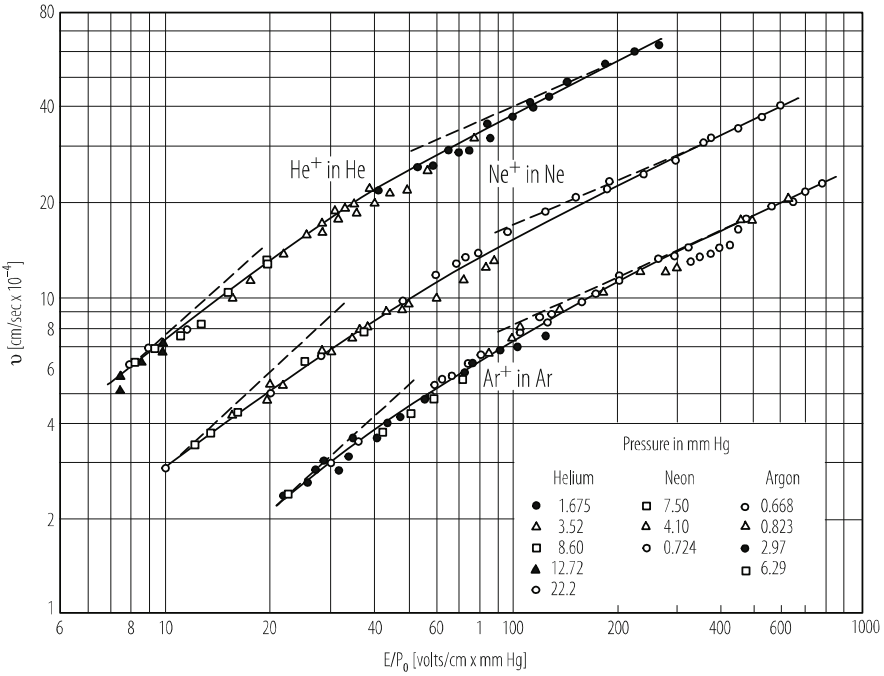

Fig. 4.7 Drift velocities of singly charged ions of noble gases [32]

In the steady state d**u**/dt = 0 and

$$\mathbf{u}/\tau - (e/m)\,[\mathbf{u}\ \mathrm{x}\ \mathbf{B}] = (e/m)\,\mathbf{E}, \tag{4.21}$$

with τ = m/k. The solution for **u** is

$$\mathbf{u} = (e/m)\,\tau \mid \mathbf{E} \mid \left(1/\left(1+\omega^2\tau^2\right)\right)\left\{\mathbf{E}^* + \omega\tau\left[\mathbf{E}^*\ \mathrm{x}\ \mathbf{B}^*\right] + \omega^2\tau^2\,(\mathbf{E}^*\mathbf{B}^*)\,\mathbf{B}^*\right\}, \tag{4.22}$$

where $\omega = (e/m) \mid \mathbf{B}\mid$, and ω carries the sign of e and $\mathbf{E}^*$ and $\mathbf{B}^*$ are unit vectors.

For ions, $\omega\tau \approx 10^{-10}$ Therefore, magnetic fields have negligible effect on ion drift.

For electrons, **u** is along **E**, if $B = 0$, with

$$\mathbf{u} = (e/m)\,\tau\mathbf{E}. \tag{4.23}$$

This is the same relation as the one derived from the microscopic picture (4.11), which provides the interpretation of τ as the *mean time between collisions*.

For large $\omega\tau$, **u** tends to be along **B**, but if **EB** = 0, large $\omega\tau$ tums u in the direction of **ExB**.

Two *special cases* are of practical interest for *electron drift*:

E orthogonal to B

With $\mathbf{EB} = 0$ and choosing $\mathbf{E} = (E_x,\ 0, 0)$ and $\mathbf{B} = (\mathrm{O},\ 0,\ B_z)$, we get

$$\begin{aligned} u_x &= (e/m)\,\tau \mid \mathbf{E} \mid / \left(1 + \omega^2\tau^2\right)\ , \\ u_y &= -\,(e/m)\,\tau\omega\tau \mid \mathbf{E} \mid / \left(1 + \omega^2\tau^2\right), \\ u_z &= 0, \end{aligned} \tag{4.24}$$

and

$$\mathrm{tg}\psi = u_y/u_x = -\omega\tau. \tag{4.25}$$

The latter relation is used to determine $\omega\tau$, i.e. τ, from a measurement of the drift angle ψ, the so-called *Lorentz angle*. In detectors, this angle increases the spread of arrival times and sometimes also the spatial spread. A small $\omega\tau$ would, therefore, be an advantage but good momentum resolution requires usually a strong B.

The absolute value of $\mathbf{u}$ is

$$\mid \mathbf{u} \mid = (e/m)\,\tau \mid \mathbf{E} \mid \left(1 + \omega^2\tau^2\right)^{-1/2} = (e/m)\,\tau \mid \mathbf{E} \mid \cos\psi. \tag{4.26}$$

This means that, independent of the drift direction, the component of $\mathbf{E}$ along $\mathbf{u}$ determines the drift velocity (Tonks' theorem). This is well verified experimentally.

E Nearly Parallel to B

This is the case in the Time Projection Chamber (TPC). Assuming E along z and the components $\mid B_X \mid$ and $\mid B_y \mid$ $<<$ $\mid B_z \mid$, one finds in first order

$$\begin{aligned} u_x/u_z &= \left(-\omega\tau\, B_y/B_z + \omega^2\tau^2 \mathrm{B_x/B_z}\right) / \left(1 + \omega^2\tau^2\right), \text{ and} \\ u_y/u_z &= \left(\omega x \mathrm{B_x/B_z} + \omega^2\tau^2 \mathrm{B_y/B_z}\right) / \left(1 + \omega^2\tau^2\right). \end{aligned} \tag{4.27}$$

In a TPC this will produce a displacement after a drift length L of $\delta_x = Lu_x/u_z$ and $\delta_y = Lu_y/u_z$ From measurements with both field polarities and different fields, B_X, B_y and τ can be determined.

If B_x and B_y can be neglected with respect to B_z, u_z remains unaffected by B.

4.2.2.2 Diffusion

Due to the random nature of the collisions, the individual drift velocity of an electron or ion deviates from the average. In the simplest case of isotropic deviations, a point-like cloud starting its drift at $t = 0$ from the origin in the z direction will at time t assume a Gaussian density distribution

$$N = (4\pi Dt)^{-3/2} \exp\left(-r^2/(4Dt)\right), \tag{4.28}$$

with $r^2 = x^2 + y^2 + (z - ut)^2$, D being the *diffusion coefficient*. In any direction from the cloud centre, the mean squared deviation of the electrons is

$$\sigma_{\mathrm{I}} = (2Dt)^{1/2} = (2Dz/u)^{1/2} = D^* z^{1/2}. \tag{4.29}$$

with D^* called *diffusion constant*. In terms of the microscopic picture, D is given by

$$D = \lambda^2/(3\tau) = c\lambda/3 = c^2\tau/3 = (2/3)(\varepsilon/m)\tau, \tag{4.30}$$

with λ being the *mean free path*, $\lambda = c\tau$, and ε the *mean energy*.

With the *mobility* μ defined by

$$\mu = (e/m)\tau, \tag{4.31}$$

the mean energy ε can be determined by a measurement of the ratio D/μ:

$$\varepsilon = (3/2)(D/\mu)e. \tag{4.32}$$

Instead of ε, the *characteristic energy* $\varepsilon_k = (2/3)\varepsilon$ is often used.

The *diffusion width* σ_x of an initially point-like electron cloud having drifted a distance L is determined by the electron energy ε:

$$\sigma_X^2 = 2Dt \;\; = 2DL/(\mu E) = (4/3)\varepsilon L/(eE) \tag{4.33}$$

This relation is used for the *determination* of D *and* ε.

For a good spatial resolution in drift chambers, a low electron energy and high electric fields are required. The lower limit for ε is the thermal energy $\varepsilon_{\mathrm{th}} = (3/2)kT$. In this limit, the relationship known as *Einstein or Nernst-Townsend formula* follows:

$$D/\mu = kT/e. \tag{4.34}$$

The *minimum diffusion width* is thus

$$\sigma_{x,\mathrm{mm}}{}^2 = (kT/e)(2L/E). \tag{4.35}$$

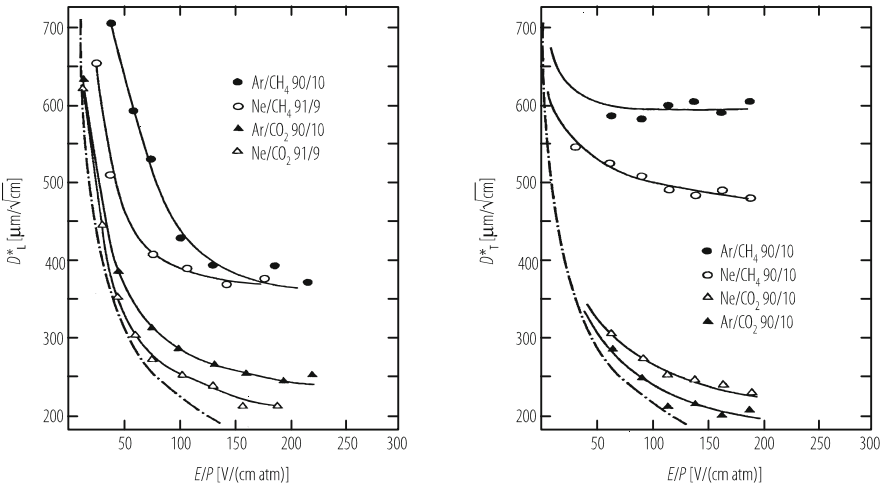

Fig. 4.8 Longitudinal and transverse diffusion constants for low electric fields [33]. The dash-dotted line denotes the thermal limit

As can be seen in Fig. 4.8, this minimum is approached for 'cold gases' like Ar/CO_2 up to E~150 V/cm at 1 atm, for 'hot gases' like Ar/CH_4 only for much lower fields.

Anisotropic Diffusion

So far, we have assumed isotropic diffusion. In 1967 it was found experimentally [34], that the *longitudinal diffusion* D_L along E can be different from the *transversal diffusion* D_T Subsequently it has been established that this is usually the case.

For ions this anisotropy occurs only at high E. As in a collision ions retain their direction to a large extent, the instantaneous velocity has a preferential direction along E. This causes diffusion to be larger longitudinally. However, this high field region is beyond the drift fields used in practical detectors.

For electrons a semi-quantitative treatment [35], restricted to energy loss by elastic collisions, shows that

$$D_L/D_T = (1+\gamma)\,/\,(1+2\gamma) \;\text{ with }\; \gamma = (\varepsilon_0/v_0)\,(\delta v/\delta\epsilon)\,. \tag{4.36}$$

It follows that longitudinal and transversal diffusion will be different, if the collision rate v depends on the electron energy ε.

Figures 4.8, 4.9, 4.10 show measured diffusion for a drift of 1 cm for some common gas mixtures [30, 33, 36]. Simulated diffusion curves are compiled in [33].

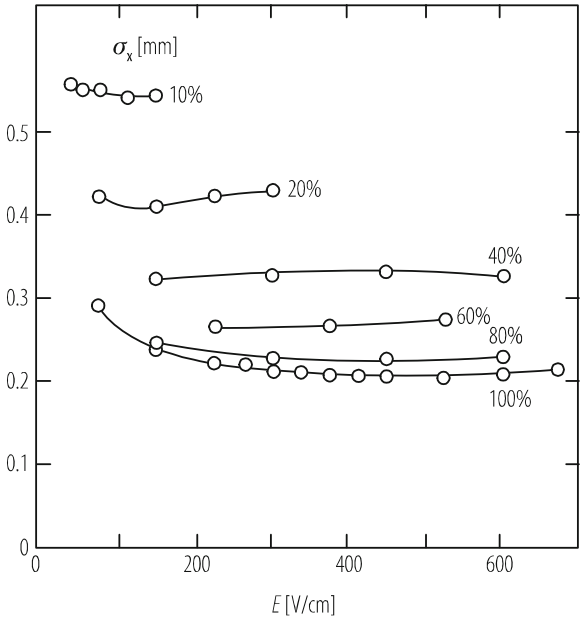

Fig. 4.9 Transverse diffusion for 1 cm drift in Ar/CH_4 mixtures; CH_4 % is indicated [36].

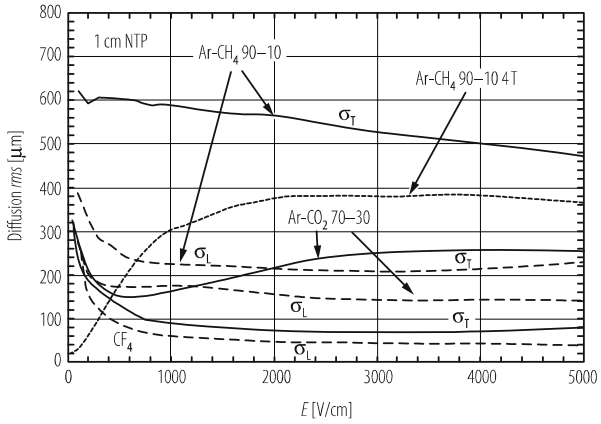

Fig. 4.10 Transverse and longitudinal diffusion for 1 cm drift up to higher E fields [30]

A *magnetic field B* along z will cause electrons to move in circles in the x-y projections in between collisions. The random propagation is diminished and the transverse diffusion will be reduced:

$$D_{\mathrm{T}}(\omega)/D_{\mathrm{T}}(0) = 1/\left(1+\omega^2\tau^2\right). \tag{4.37}$$

This reduction is essential for most TPCs with their long drift distances.

A more rigorous treatment of averages [19] shows that different ratios apply to low and high B:

$$\begin{aligned} D(0)/D(B) &= 1 + \omega^2\tau_1^2 \quad \text{for low } B, \text{ and} \\ D(0)/D(B) &= C + \omega^2\tau_2^2 \quad \text{for high } B. \end{aligned} \tag{4.38}$$

This behaviour was indeed verified [37], by measuring $D(B)$ over a wide range of B. In an Ar/CH_4 (91/9%) mixture the data could be fitted with $\tau_1 = 40$ ps, $\tau_2 = 27$ ps and $C = 2.8$. The high field behaviour is approached above about 3 kg, close to $\omega\tau = 1$.

The longitudinal diffusion remains unchanged: $D_L(\omega) = D_L(0)$.

The effects of E and B combine if both fields are present.

4.2.2.3 Electron Attachment

In the presence of electronegative components or impurities in the gas mixture, the drifting electrons may be absorbed by the formation of negative ions. Halogenides (e.g. CF_4) and oxygen have particularly strong electron affinities. Two-body and three-body attachment processes are distinguished [38].

In the *two-body process*, the molecule may or may not be broken up:

$$\begin{aligned} &e^- + AX \rightarrow Ax^-* \rightarrow A \ (\text{or } A^*) + X^- \left(\text{or } X^-*\right) \text{ or} \\ &e^- + AX \rightarrow Ax^-* \rightarrow AX^- + \text{energy}. \end{aligned} \tag{4.39}$$

The attachment rate R is proportional to the density N:

$$R = c\sigma N \tag{4.40}$$

for an electron velocity c and attachment cross-section σ The rate constants of freons and many other halogen-containing compounds are known [39].

The best known three-body process is the Bloch-Bradbury process [40]. In this process, an electron is attached to a molecule through the stabilizing action of another molecule. It is important for the attachment of electrons with energy below 1 eV to O_2, forming an excited unstable state with a lifetime τ of the order of 10^{-10} s. A stable ion will be formed only if the excitation energy is carried away during τ by another molecule. The attachment rate is proportional to the square of the gas pressure, as it depends on the product of the concentrations of oxygen and of the stabilizing molecules [19]:

$$R = \tau c_e c_2 \sigma_1 \sigma_2 N\,(O_2)\, N\,(X)\,. \tag{4.41}$$

Here c_e is the electron velocity, c_2 the relative thermal velocity between O_2 and X In an Ar/CH_4 (80/20%) mixture at 8.5 atm with an O_2 contamination of 1 ppm, an absorption of 3%/m was measured at a drift speed of 6 cm/μs.

4.2.3 Avalanche Amplification

4.2.3.1 Operation Modes

Gas detectors generally use gas amplification in the homogeneous field of a parallel plate geometry or, more frequently, in the inhomogeneous field around a thin wire. We shall start with the discussion of the second case.

Near a wire with a charge q_s per cm, the electric field at a distance r from its centre is

$$E = q_s / (2\pi\varepsilon_0 r) . \tag{4.42}$$

When raising the field beyond the *ionization chamber regime*, in which all primary charges are collected *without* any *amplification*, at some distance from the wire a field is reached, in which an electron can gain enough energy to ionize the gas and to start an avalanche. The avalanche will grow until all electrons have arrived on the anode wire. For a *gas amplification A* of $1000 \sim 2^{10}$, some 10 ionization generations are required. As the mean free path between collisions is of the order of microns, the field to start an avalanche has to be several times 10^4 V/cm. This is usually achieved by applying a voltage of a few kV to a thin wire, with a diameter in the $20 - 50$ μm range.

Besides ionization, *excitation* will always occur and with it photon emission. A fraction of these photons may be energetic enough to produce further ionization in the gas or on the cathode. Only those photons which ionize outside the radius r_{av} of the moving electron avalanche may be harmful, as their avalanches will arrive later. If γ called the *second Townsend coefficient*, is the probability per ion pair in the first avalanche to produce one new electron, and if A denotes the amplification of the first avalanche, *breakdown* will occur for

$$A\gamma > 1. \tag{4.43}$$

In this case the first avalanche will be followed by a bigger one, this by an even bigger and so on, until the current is limited by external means. If $A\gamma << 1$, $A\gamma$ gives the probability for producing an after-discharge. If a photoionization takes place inside r_{av}, the effect will be an increase of A.

The resulting need to suppress far-traveling photons produced in the rare gases is the reason for the use of 'quench gases' like Methane, Ethane, CO_2, etc., which have large absorption coefficients for UV photons.

The positive ions produced in the avalanche have too little energy to contribute to the ionization in the avalanche. They will move slowly to the cathode(s), where they get neutralized but where rare gas ions may also liberate additional electrons. The addition of the quencher reduces this risk significantly, as its recombination energy can be dissipated in other ways, e.g. by disintegration. This explains why more complex molecules provide higher protection.

Up to a certain value A_p, one has a *proportional regime*: the signal produced will on average be proportional to the number of primary electrons. The amplification will rise approximately exponentially with voltage. The azimuthal extension of the avalanche around the wire will grow with amplification and eventually the avalanche will surround the wire.

When the field is raised above this proportional regime, *space charge effects* will set in. The space charge of the positive ions—moving only very slowly compared to the electrons—will reduce the field at the head of the avalanche and the amplification will rise more slowly with voltage and will no longer be proportional to the primary ionization. In addition, space charge effects will depend on the track angle with respect to the wire and on the density of the primary ionization. This is the so-called *limited proportionality regime*.

Increasing the field further, the positive space charge may produce additional effects. Near the avalanche tail the electric field is increased. If the absorption of UV photons in the quench gas is high, the photons may ionize this high field region and start a *limited streamer* moving backwards by starting avalanches further and further away from the sense wire. As the electric field at large radius weakens, this development will stop after typically 1–3 mm. The total charge is almost independent of the primary charge starting the streamer. The process depends quite strongly on experimental conditions. An example is presented in Fig. 4.11, which shows a steep step from the proportional regime [41]. In the narrow transition zone one finds a rapid change of the ratio of streamer/proportional signal rates. In other experimental conditions a smoother transition has been observed.

If the absorption of the UV photons is weak, photons travel further and avalanches may be started over the full length of the wire, leading to the *Geiger mode*, if the discharge is limited by external means.

4.2.3.2 Gas Gain

With multiplication, the number n of electrons will grow on a path ds by

$$\mathrm{d}n = n\ \alpha\ \mathrm{d}s, \tag{4.44}$$

where α is the *first Townsend coefficient*. Ionization growth is obviously proportional to the gas density p and depends on the ionization cross-sections, which are a function of the instantaneous energy ε of the electrons. This energy itself is a function of E/p. The relationship between α and E is, therefore, given in the form α/p as function of E/p or for a specific temperature as $\alpha/p(E/p)$. Figure 4.12 gives some

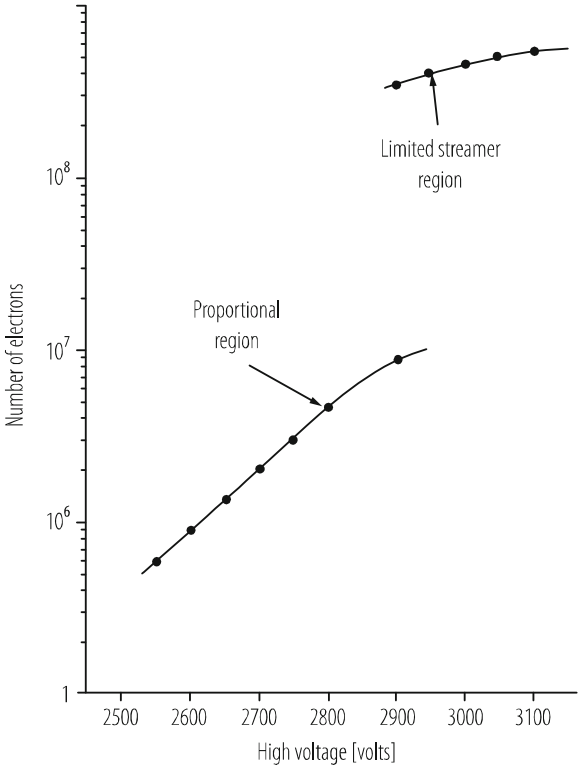

Fig. 4.11 Pulse-height transition from limited proportionality to limited streamer mode [41]

examples of measurements [42]; it shows the strong increase of α with electric field in the region of interest to gas detectors, up to about 250 kV/cm. No simple relation exists for α as function of electric field E, but Monte Carlo simulation has been used to evaluate α. Figure 4.13 shows an example [27]. For the lower field values there is reasonable agreement with measurement. The discrepancy at the highest fields is attributed to photo-and Penning-ionization not being included.

The amplification A in the detector is obtained by integration

$$A = n/n_0 = \exp \int \alpha(s)\, \mathrm{d}s = \exp \int \alpha(E)/\left(\mathrm{d}E/\mathrm{d}s\right) \mathrm{d}E, \tag{4.45}$$

from $E_{\min}$, the minimum field to start the avalanche, to the field $E(a)$ on the wire. $E_{\min} e$ is equal to the ionization energy of the gas molecules divided by the mean free path between collisions. Near the wire and far from other electrodes, the field is

$$E(r) = q_s/\left(2\pi r \varepsilon_0\right), \tag{4.46}$$

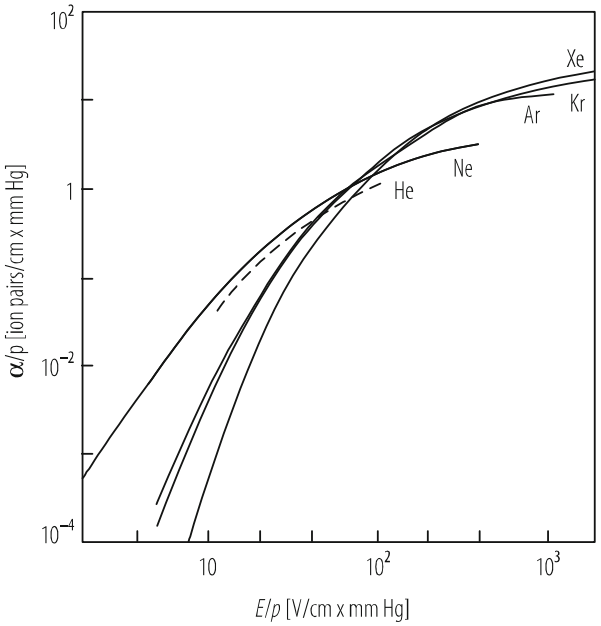

Fig. 4.12 Examples of measured 'First Townsend coefficient' α in rare gases [42]

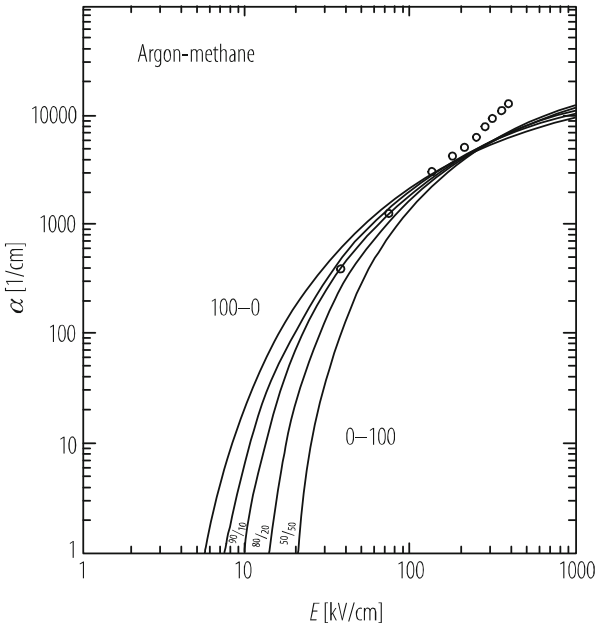

Fig. 4.13 Simulated 'First Townsend coefficient' α in Ar/CH_4 mixtures at 1 atm (100–0 means 100%Ar). Measured values are indicated as circles [27]

where q_s is the charge per cm. Therefore,

$$A = \exp \int q_s \, \alpha(E) \, \mathrm{d}E / \left(2\pi \varepsilon_0 E^2\right). \tag{4.47}$$

Two approximations in particular have been used to describe practical cases.
The early *Korff model* [43] uses the parameterization

$$\alpha / p = A \exp\left(-Bp/E\right), \tag{4.48}$$

with empirical constants A and B depending on the gas.

In the *Diethorn approximation* [44], α is assumed to be proportional to E. One then obtains for a proportional tube with wire radius a and tube radius b

$$\ln A = \left(\ln 2 / \ln\left(b/a\right)\right) \left(V/\Delta V\right) \ln\left(V / \left(\ln\left(b/a\right) a E_{\min}\right)\right), \tag{4.49}$$

where the two parameters E_{mm} and ΔV are obtained from measurements of$A$ at various voltages and gas pressures. E_{mm} is the minimum E field to start the avalanche and $e\Delta V$ the average energy required to produce one more electron. E_{mm} is defined for a density p_0 at STP. For another density $E_{\mathrm{mm}}(p) = E_{\mathrm{mm}}(p_0)(p/p_0)$. A list for E_{mm} and ΔV for various gases is given, e.g., in [19]. Reasonable agreement with the experimental data is obtained; discrepancies show up at high A.

4.2.3.3 Dependence of Amplification on Various Factors

The gas amplification depends on many operational and geometrical parameters. Some examples are:

Gas Density

The Diethom approximation gives

$$\mathrm{d}A/A = -\left(\ln 2 / \ln\left(b/a\right)\right) \left(V/\Delta\nabla\right) \left(\mathrm{d}p/p\right) \rightarrow = \text{(5-8)} \;\; \mathrm{d}p/p \tag{4.50}$$

typically.

Geometrical Imperfections

The effects will obviously depend on the geometry and the operation details. An early publication [45] gives analytic estimates of the effects of wire displacements and variations in wire diameter. In a typical geometry $\mathrm{d}A/A \sim 2.5\, \mathrm{d}r/r$, where r is the wire radius; $\mathrm{d}A/A \sim 9 \Delta gap/gap$.

Edge Effects

Near edges, the electric field is reduced over distances similar to the gap between the electrode planes. It can be recovered largely by additional field shaping lines on the edges [46].

Space Charge

Due to the low velocity of the positive ions (falling off as $1/r$ from >1mm/μs at $r = a$), space charge will build up at high particle fluxes and lower the avalanche amplification. In drift tubes the voltage drop due to the space charge from a given particle flux is proportional to the third power of the tube radius. A smaller radius thus improves the rate capability drastically.

4.2.3.4 Statistical Fluctuations of the Amplification

In the proportional regime, the amplification A is simply defined by $A = n/n_{\mathrm{T}}$ and one assumes that each of the n_{T} initial electrons produces on average the same A ion pairs. We define $P(n)$ as the probability to produce n electrons in the individual avalanche with mean A and variance σ^2 If $n_{\mathrm{T}} > > 1$ and if all avalanches develop independently, it follows from the central limit theorem that the distribution function $F(n)$ for the sum of the n_{T} avalanches approaches a Gaussian with mean $n = n_{\mathrm{T}}A$ and variance $S^2 = n_{\mathrm{T}}\sigma^2$, independent of the actual $P(n)$.

On the other hand, for detection of single or a few electrons, knowledge of the individual $P(n)$ is required.

For a parallel plate geometry calculations [47] agree well with measurements [48]. The distributions found theoretically [49] and experimentally [50] for the strong inhomogeneous field around a thin wire also look similar and approach Polya distributions (Fig. 4.14).

For these distributions

$$(\sigma_A / < A >)^2 = f, \text{with } f \leq 1. \tag{4.51}$$

The limiting case $f = 1$ is an exponential distribution (Yule-Furry law)

$$P(A) = (1/ < A >) \exp(-A/ < A >). \tag{4.52}$$

Experimental results point to $f = 0.6 - 1.0$. Measurements with laser tracks [19], indicate that the r.m.s. width σ_A of a single-electron avalanche is close to the mean, as it is for the Polya distribution with $f = 1$. An approximately exponential distribution for single-electron avalanches is also reported in [28, 48].

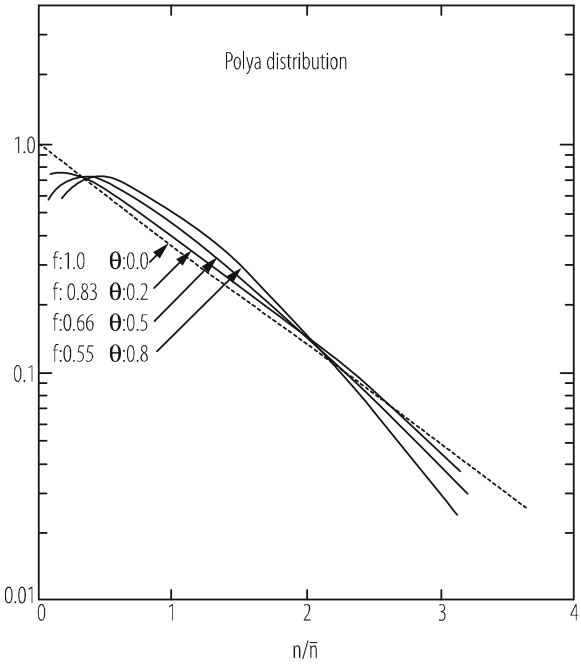

Fig. 4.14 Polya distributions [22]

4.2.4 Signal Formation

In wire chambers, signal formation is very similar to the one in the simplest geometry of a cylindrical tube with a coaxial wire, because most of the useful signal is produced in the immediate vicinity of the sense wire and the electric field around the sense wires in a MWPC can be considered as radial up to a radius equal to about one tenth of the distance between sense wires [45].

Signals are *always* produced *by induction* from the moving charges.

Ramo [51] and Shockley [52] have shown that in general the current I_R induced on the readout electrode R is given by

$$I_R = -q\ \mathbf{E}_w \mathbf{v}, \tag{4.53}$$

where q is the signed charge moving with the vectorial velocity $\mathbf{v}$, and $\mathbf{E}_w$ is a vectorial *weighting field*, a conceptual field defined by applying + 1V on R and 0 V on all other electrodes. The unit of E_w is 1/cm. The actual v is calculated by applying the normal operation voltages, including possibly a B field.

In the special case of a two electrode system like the wire tube, $\mathbf{E}_w = \mathbf{E}_{op}/V$, where $\mathbf{E}_{op}$ is the actual operating field obtained with the voltage V on R (the anode wire) and zero V on the cathode.

For the proportional tube with wire radius a and cathode radius b, E_{op} and E_{w} are obviously radial with

$$E_{\mathrm{op}} = V/\left[r \ln\left(b/a\right)\right]. \tag{4.54}$$

We assume constant mobility μ for the positive ions. Therefore

$$v^{+}\left(\mathrm{t}\right) = \mu V/\left[r(t) \ln\left(b/a\right)\right]. \tag{4.55}$$

For an ion starting at $t = 0$ from $r = r_1$,

$$r(t) = r_1(1 + (t/t_0))^{1/2} \text{ with } t_0 = r_1^2 \ln\left(b/a\right) / \left(2\mu V\right). \tag{4.56}$$

The maximum time for an ion to drift from a to b is

$$T^{+}{}_{\max} = (b/a)^2 t_0, \text{ as } (b/a)^2 >> 1. \tag{4.57}$$

The induced current I^{+} is

$$I^{+} = -q\ \mathbf{E}_{\mathrm{w}}\mathbf{v}^{+} < 0, \tag{4.58}$$

as $\mathbf{v}^{+}$ is parallel to $\mathbf{E}_{\mathrm{w}}$.

For the integrated charge Q, one obtains

$$Q^{+}(t) = \int I\ \mathrm{d}t = \int I\left(1/v^{+}\right)\ \mathrm{d}r = \int -qE_{\mathrm{w}}\ \mathrm{d}r. \tag{4.59}$$

Integration from r_1 to r_2 gives

$$Q^{+}{}_{1\to 2} = -q \ln\left(r_2/r_1\right) / \ln\left(b/a\right), \text{ with } q > 0 \text{ and } r_2 > r_1, \tag{4.60}$$

For an electron one obtains

$$Q^{-}{}_{1\to 2} = +q \mid \ln\left(r_2/r_1\right) \mid / \ln\left(b/a\right), \text{ with } q < 0 \text{ and } r_2 < r_1, \tag{4.61}$$

as $\mathbf{v}$ is antiparallel to $\mathbf{E}_{\mathrm{w}}$.

We shall give numbers for a typical proportional tube with $a = 10\ \ \mu\mathrm{m}$, $b = 2.5$ mm, $E_{\mathrm{op}}(r = a) = 200\ \ \mathrm{kV/cm}$, $\mu^{+} = 1.9\ \mathrm{atm\ cm^2/(Vs)}$, $\mathrm{v}^{-} \approx 5 \cdot 10^6\ \ \mathrm{cm/s}$ and—to estimate the gas amplification A—the Diethom parametrization $\alpha = (\ln 2/\Delta\nabla)E$ and $E_{\min} = V/(r_{\mathrm{mm}} \ln\left(b/a\right))$, taking for an $\mathrm{Ar/CH_4}$(90/10) mixture $\Delta V = 23.6\,\mathrm{V}$ and $\mathrm{E}_{\min} = 48\ \mathrm{kV/cm}$ [19], p. 136. Here r_{mm} is the starting radius for the avalanche and $E_{\min}$ the minimum field permitting multiplication. We obtain: $t_0 = 1.3$ ns, $T^{+}_{\max} = 82\ \mu\mathrm{s}$, $r_{\min} = 42\,\mu\mathrm{m}$, $A = 4400$.

The last electron will be collected in a very short time of about 0.6 ns, the vast majority even faster. Half of the electrons move only about 2 μm, the next 25%

some 4 μm and so on. A rough estimate of the induced electron charge signal is, therefore,

$$Q^{-}{}_{\text{total}} = q \ln(14/10) / \ln(2500/10) = 0.06\, q. \tag{4.62}$$

Only about 6% of the total induced signal is due to the movement of the electrons, the rest from the ions, if one integrates over the full ion collection time.

In practice, however, one mostly uses much faster integration. The long tail in the signal caused by the very slow ion movement has to be corrected for by electronic pulse shaping to avoid pile-up at high rates (see Sect. 4.69). If one uses fast pulse shaping, say 20 ns integration, only a fraction of the ion charge will be seen: an ion starting at $r_1 = a$, reaches $r_2 = 40\,\mu\text{m}$ in 20 ns and induces about 25% of its charge. That means: with 20 ns pulse shaping, one may expect to see an *effective charge* of about 30% of the total charge produced, of which one fifth is due to the electrons.

4.2.5 Limits to Space Resolution

The space resolution σ_X obtained from a single measurement of the anode wire signals in a multi-wire proportional chamber is given by the separation s of the wires: $\sigma_x = s/\sqrt{12}$. The minimum practical s for small chambers is 1 mm. The best resolution is thus about 300 μm.

Significantly better resolution may be obtained either from 'centre of gravity' determination or from the electron drift times in drift chambers.

4.2.5.1 'Centre of Gravity' Method

In this method one uses the signals induced on cathode strips or pads, see Fig. 4.19. The rms width of the induced charge distribution is comparable to the anode-cathode gap d. If one chooses a strip width of (1–2)d, one obtains signals above threshold on typically 3–5 strips. Depending on the signal to noise ratio, a resolution of typically (1–5)% of the strip width is achieved, i.e. about $40 - 100\,\mu\text{m}$. This method is used for the read out of TPCs, as well as for high precision cathode strip chambers, see e.g. [15, 16].

4.2.5.2 Drift Time Measurement

The main contributions to the error of the drift time determination come from electronics noise, electron clustering, δ-rays, diffusion. This assumes that additional effects on the space-time correlation including magnetic field corrections, gain variations, gas contamination and others are kept small by careful construction and calibration. Figures 4.16 and 4.24 (*right*) show typical results. Electronic noise

contributes a constant error. Near the anode wire, the effects of the clustering of the primary charges adds a significant error. At large distances from the anode, the contribution from diffusion grows as square root of distance. Resolutions achieved are typically $50 - 200\,\mu\text{m}$.

A detailed discussion of limits to space resolution is presented in [19] and for the particular case of proportional tubes in [15].

4.2.6 Ageing of Wire Chambers

Deterioration of performance with time has been observed since the early days of gas detectors but has gained importance with the ever increasing radiation loads due to the demand for higher detection rates over long periods. Typical effects of *ageing* are: pulse height decrease, a broadening of the energy resolution and increase in dark current, in the extreme also electrical breakdown or broken wires. An enormous number of studies has been carried out. They are well documented in the proceedings of workshops [54] and several reviews [55].

Upon opening of damaged chambers, deposits have been observed on anode wires and/or on cathodes. On the wire they can take any form from smooth layers to long thin whiskers [56], see Fig. 4.15. On the cathodes, deposits usually consist in spots of thin insulator. Defects of this latter kind can often be correlated with a discharge pattern, which may be interpreted as Malter effect [57]: under irradiation, charges build up on the insulator until the electric field is strong enough to extract electrons from the cathode through the layer into the gas where they initiate new avalanches. The facts that the buildup time decreases with higher ionization rate and that the discharges take some time to decay after irradiation is timed off, give support to this explanation, as does the observation that addition of water vapour is reducing the discharges, probably introducing some conductivity.

Analysis of the layers and whiskers on the anode wires often indicate carbon compounds, more surprisingly also often silicon, sometimes other elements: Cl, O, S.

The aging results are often characterized by a drop in pulse height ΔPH as function of integrated charge deposition in Coulomb per cm wire, although it was found in some cases that the rate of the charge deposition has an influence. Typical values with classical gas mixtures containing hydrocarbons are

$$\begin{aligned} \Delta PH/PH &\sim 0.01 - 0.1\%/0/\text{mC/cm} \quad \text{for small detectors,} \\ \Delta PH/PH &\approx 0.1 - 1\%/\text{mC/cm} \qquad\quad \text{for large detectors.} \end{aligned} \tag{4.63}$$

It is obvious that the control of ageing is one of the major challenges for the LHC experiments, possibly even the major one.

Unfortunately, however, it has not been possible to establish a common fundamental theory, which could predict lifetimes of a new system. On the other hand, the

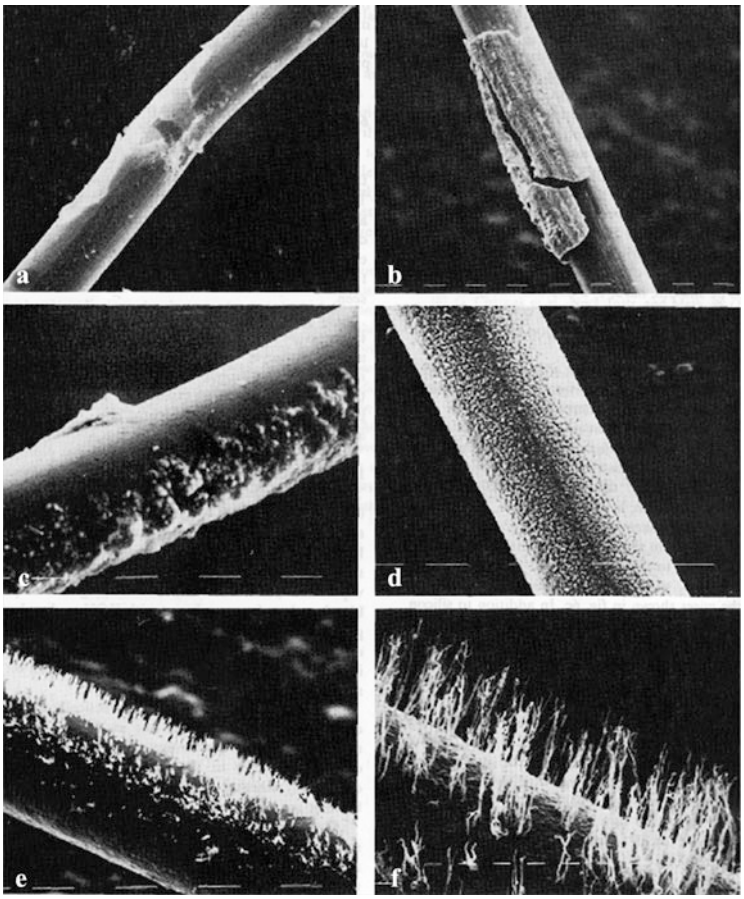

Fig. 4.15 Examples of deposits on 20 μm anode wires after strong irradiation [56]

reasons for ageing in particular circumstances have been elucidated and the studies permit to establish *some general rules* on how for improving the chances for a longer lifetime:

- *Many materials have to be avoided*, in the gas system, in the detector and during the construction: Si compounds, e.g. in bubbler oils, adhesives, vacuum grease or protection foils, PVC tubing, soft plastics in general, certain glues and many more. The workshop proceedings and reviews mentioned present details, also on materials found acceptable.
- For the highest radiation loads, up to a few C/cm, gas components most frequently used in the past, namely *hydrocarbons* like Methane, Ethane, etc., *should be avoided*. Indeed, the LHC experiments make use of them only exceptionally. There remains only a very restricted choice of acceptable gases: mixtures of rare gases and CO_2 and possibly N_2, CF_4 or DME. CF_4 is offering high electron drift

velocities and has proven to be capable under certain conditions to avoid or even to etch away deposits, in particular in the presence of minute Si impurities. But its aggressive radicals may also etch away chamber components, especially glass [15]. In any case the water content has to be carefully controlled to stay below 0.1%, if CF_4 is used, to avoid etching even of gold-plated wires. Also DME, offering low diffusion, has in some cases provided long lifetime. It has, however, shown to attack Kapton and to be very sensitive to traces of halogen pollutants at the ppb level.

- During production, *high cleanliness* has to be observed, e.g. to avoid resistive spots on the cathodes. The sense wire has to be continuously checked during wiring to assure the required quality of its geometrical tolerances and of the gold plating.
- The gas amplification should be kept as low as possible.
- In any case, a final detector module with the final gas system components should be extensively tested under irradiation. As an accelerated test is usually required for practical reasons, to obtain the full integrated charge for some 10 years of operation in a 1 year test, an uncertainty un- fortunately will remain, because a rate dependence of the ageing cannot be excluded.

4.3 Detector Designs and Performance

4.3.1 Single Wire Proportional Tubes

Despite the revolution started with the multiwire proportional chambers (MWPC), single wire tubes are still widely used, mostly as drift tubes. They have circular or quadratic cross-section and offer independence of the cells, important, e.g., in case wire rupture. We present three examples.

ATLAS has chosen for the muon system *large diameter* (*3 cm*) *aluminum tubes* operated with Ar/CO_2 (93/7%) at 3 atm, with the addition of about 300 ppm of water to improve HV stability. A pair of 3 or 4 staggered tube layers, separated by a support frame, form a module. The disadvantages of the gas mixture, a non-linear space-drift time relation and relatively long maximum drift time, had to be accepted in order to obtain a high radiation tolerance. The spatial resolution for a single tube under strong γ- irradiation producing space charge is shown in Fig. 4.16. An average resolution per tube of 80 μm is expected with a maximum background rate of 150 hits/cm^2 s. With a relative positioning of the wires during construction to 20 μm, an adjustment of the tube curvature to the gravitational wire sag and a relative alignment and continuous monitoring of the pair of layers inside a chamber, a combined resolution for the 6–8 1ayers of ~35 μm is aimed at. These chambers provide only one coordinate, the other one being measured in other subdetectors of the experiment.

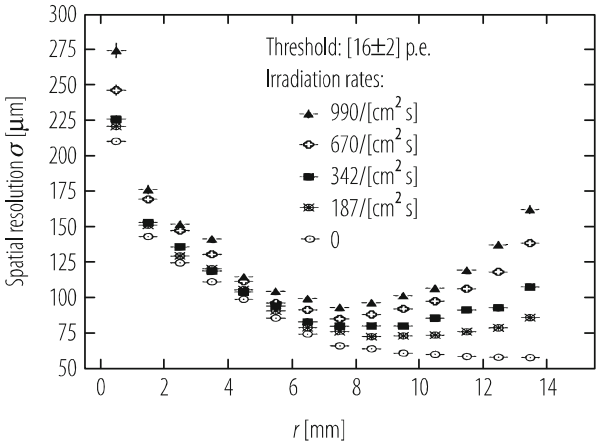

Fig. 4.16 ATLAS MDT drift tubes: space resolution as function of impact radius and background rates. Expected rates are $\leq$150 hits/cm^2 s [15]

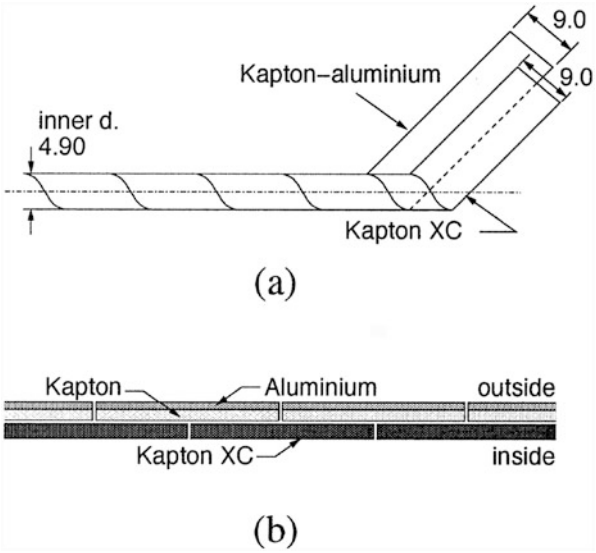

Fig. 4.17 LHCb straw tubes: (**a**) Winding scheme. (**b**) Details of the double foil. Kapton XC is on the inside [17]

A second type of tube design, *straw tubes*, has become very popular since a number of years. Straw tubes offer high rate capability due to small diameters and relatively little material in the particle path. In LHCb, where local rates (near one end of the wire) up to 100 kHz/cm have to be handled, an internal diameter of 4.9 mm was chosen [17], with a construction shown in Fig. 4.17. Two strips of thin foils are wound together with overlap. The inner foil, acting as cathode, is made

of 40 μm carbon doped polyimide (Kapton-XC), the outer is a laminate of 25 μm polyimide, to enhance the gas tightness, and 12.5 μm aluminum, to ensure fast signal transmission and good shielding. The tubes are up to 2.5 m long and have the 25 μm wire supported every 80 cm.

Staggered double layers tubes are glued to light support panels to form modules up to 5 m long. An average spatial resolution of a double layer below 200 μm was measured with Ar/CO_2 (70/30%). In a station, 4 double layers are aligned along $0, +5, -5, 0^\circ$, thus providing a crude second coordinate measurement.

In another design for ATLAS [15], mechanical strengthening of 4 mm straws is achieved with carbon fibers wound around the tubes and straightness by supporting them every 25 cm with alignment planes vertical to the straws. This construction reduces the material along the radial tracks, which is essential for the role of the straws to detect transition radiation originating in fibers stacked in between the tube layers. This role also determines the need for Xe in a mixture of $Xe/CO_2/O_2$ (70/27/3%), the oxygen addition increasing the safety margin against breakdown.

Another quasi-single wire design is that of *plastic streamer tubes* usually called *Iarocci tubes*. Because they are easy to construct in large size and cheap, they have been widely used, especially as readout planes in hadron calorimeters.

A plastic extrusion with an open profile with typically 8 cells of lxl cm^2 and a PVC top plate, is coated on the inside with graphite with a minimum resistivity of 200 kΩ/square. All this is slid into a plastic box, which serves also as gas container. For stability, wires are held by plastic spacers every 50 cm. Using a thick wire of 100 μm, self-quenching streamers are initiated in a gas containing a strong quencher, typically isobutane in addition to Ar. Electrodes of any shape placed on one or both external surfaces pick up the rather strong signals. The dead time is long but only locally, so that particle rates up to 100 Hz/cm^2 can be handled.

4.3.2 Multiwire Proportional Chambers (MWPC)

Already 1 year after the invention of the multiwire proportional counter (MWPC) by Charpak in 1968, a system of small chambers was used in an experiment [58], another year later a large chamber 2 m × 0.5 m had been tested with Ar/Isobutane [59]. A number of developments like bi-dimensional readout were discussed [60]. In 1973 already, a large system of MWPC containing 50,000 sense wires had been constructed for an spectrometer at the ISR, the *Split-Field Magnet* (SFM) [61]. All these chambers had a geometry for the sense wires and gap size similar to the *original design*, shown in Fig. 4.18.

The SFM chambers of 2 × 1 m^2 contained three light support panels forming two amplification gaps of 2 × 8 mm each, one with vertical, the other with horizontal wires of 20 μm diameter. The cathodes on the panels were sprayed with silver paint to provide readout strips 5.5 cm wide and at angles of $\pm 30^\circ$, to resolve ambiguities. Special emphasis was put on high precision with a light construction, including frames of only 5 mm thickness. A total thickness of 1.7% of a radiation length

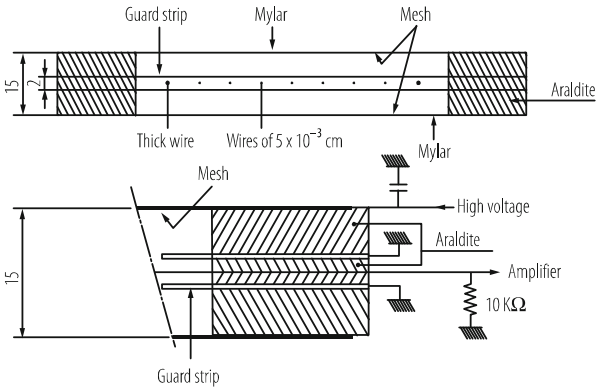

Fig. 4.18 Design of the first multiwire proportional chamber [8]

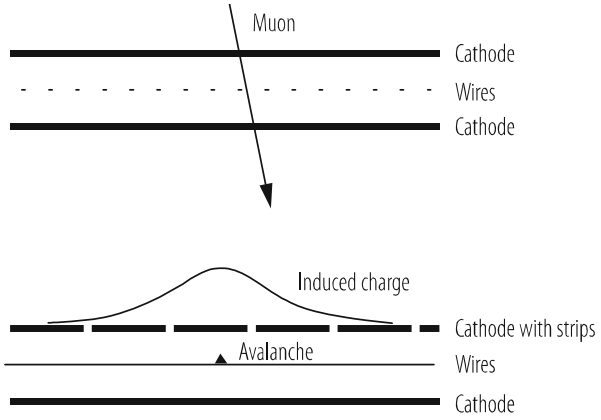

Fig. 4.19 Principle of 'centre of gravity' cathode measurement of cathode strip signals

per chamber was achieved. The stringent quality demands can be inferred from the definition of the *efficiency plateau*: the 'beginning of plateau' was defined as efficiency ε 99.98% and the end by 10 times the 'normal noise', corresponding to cosmics rate With this tight definition, the measured plateau length for a chamber was $50 - 100$ V with the magic gas mixture of Ar/isobutane/freon/methylal (67.6/25/0.4/7%).

In the following decades, drift chambers imposed themselves more and more, but MWPCs remained valid options, especially when speed was more important than high spatial resolution. Thus three of the four LHC experiments employ MWPCs, for triggering and momentum measurements. All of them make use of the signals induced on the cathode strips. In ATLAS and CMS, who call their chambers cathode strip chambers (CSC), a high precision measurement is obtained in the bending coordinate by determining the 'centre of gravity' of the strip signals, see Fig. 4.19. In ATLAS, each third strip is read out (pitch ~5.5 mm), leaving two strips floating,

and a resolution of 60 μm is obtained [15, p. 178]; in CMS, 75 μm resolution is achieved with each strip read out at a minimum pitch of 8.4 mm [16, p. 197]. In LHCb, spatial resolution is secondary to fast timing and high efficiency for a five-fold coincidence trigger. Adjustment to the requirements on spatial resolution, which change strongly with radius, is achieved by forming readout pads of variable size ($0.5 \times 2.5 - 16 \times 20$ cm^2) on the cathodes and by grouping sense wires [17, p. 130].

4.3.3 Drift Chambers

Already in the very first publications, the basic two types of drift chambers were described: (i) with the drift volume, through which the particles pass, separated from the amplification volume [9] and (ii) a geometry, in which the particles pass directly through the volume containing the anode wires alternating with field wires to improve the drift field [10], see Fig. 4.20.

The first design finally evolved into the TPC, the second into a large number of different designs. One can differentiate between planar and cylindrical geometries.

4.3.3.1 Planar Geometries

Most planar geometries are rather similar to each other. To obtain a more homogeneous drift field, additional field shaping electrodes are introduced, see Fig. 4.21. Also shown is a recent example, one element of a layer for the Barrel Muon system of CMS. The space resolution per layer is about 250 μm. One muon station consists of 2×4 layers of such tubes fixed to an aluminum honeycomb plate. The other coordinate is provided by a third set of 4 layers oriented at 90°.

The central detector of UAl used a special arrangement, see Fig. 4.22. In a horizontal magnetic field, at right angle to the beam, a cylinder 6 m long and 2.2 m in diameter is filled with planar subelements. In the central part, vertical anode planes

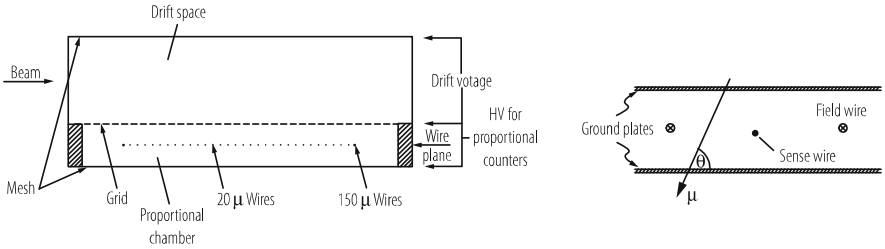

Fig. 4.20 First two drift chamber designs. *Left*: separate drift and amplification gaps [9]. *Right*: Common drift and amplification volume. The additional field wires improve the drift field [10]

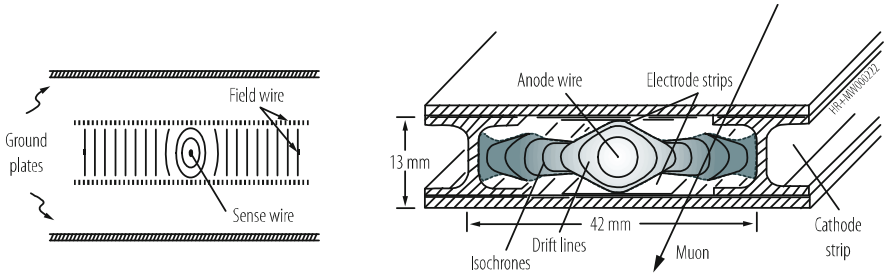

Fig. 4.21 Planar arrangement with field shaping electrodes. *Right*: cross-section of large drift tubes for CMS [16]

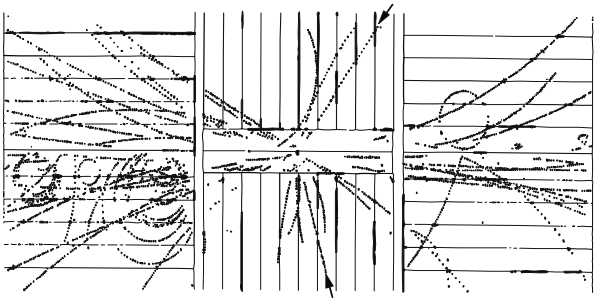

Fig. 4.22 Horizontal view of a reconstructed event in the central detector of UAl. The first Z° decay observed [19]

ultimate with cathode planes, leaving 18 cm drift spaces. These planes are horizontal in the two ends. Charge division is used for the coordinate along the wire. The average point accuracy along the drift direction was 350 μm.

4.3.3.2 Cylindrical Geometries

Many different arrangements have been worked out. Figure 4.23 shows an example of a wire arrangement and electron drift lines following the electric field in the absence of a magnetic field. The change of the electron drift in a magnetic field in a similar cell is indicated to the right.

Figure 4.24 (*left*) shows the conceptual design of the drift chamber for OPAL [53], a wire arrangement called *Jet Chamber*. The left-right ambiguity is solved by staggering the sense wires alliteratively by ±100 μm. The measured space resolution in $r\phi$ for a single wire is presented in Fig. 4.24 (*right*). The figure shows the typical dependence on the distance r from the sense wire: for small r, the primary ion statistics dominates, at large r diffusion. In addition, there is a constant contribution from the noise of the electronics. The coordinate along the wires is

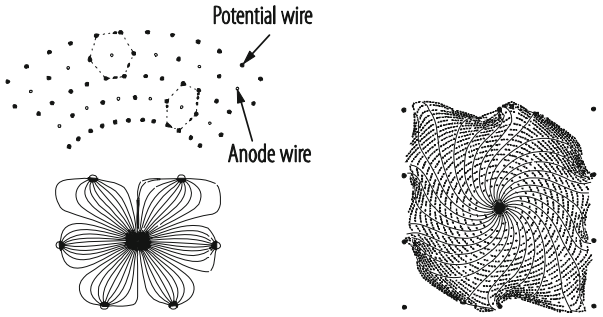

Fig. 4.23 Two multi-layer wire arrangements and electron drift lines without (*left*) and with (*right*) magnetic field

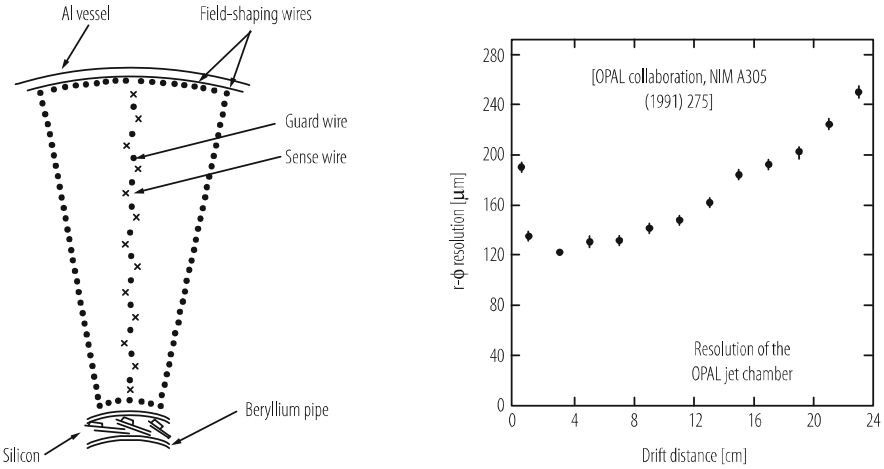

Fig. 4.24 Jet Chamber. *Left*: conceptual design with staggered sense wires. *Right*: Space resolution obtained in OPAL with 4 atm [53]

obtained from *charge division* by using resistive sense wires and read-out on both ends of the wires: a resolution of about 1% of the wire length is reached.

In other designs the *second coordinate* is obtained from orienting successive layers in stereo angles. Sometimes relative timing with read-out of both ends of the wire is used, providing again a resolution of about 1% of the wire length.

4.3.3.3 Time Projection Chambers (TPC)

The TPC concept proposed by Nygren [62] in 1974 for the PEP4 experiment [63] offered powerful pattern recognition with *many unambiguous 3-D points* along a track and particle identification by combining dE/dx information from many samples with momentum measurement. Originally proposed to resolve jets at a low

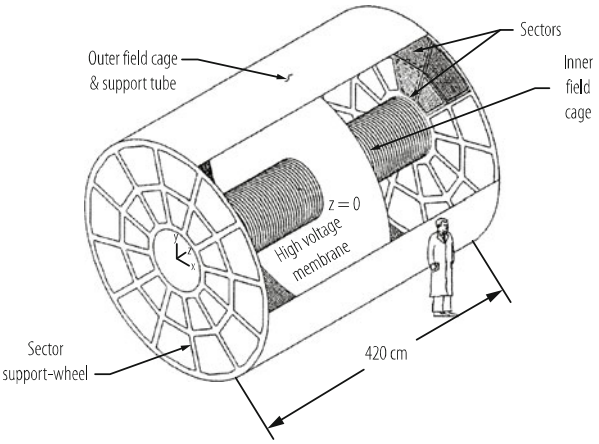

Fig. 4.25 Conceptual design of the STAR TPC operating at RIC [64]

energy e^+e^- collider, the TPC design has proven years later to be the most powerful tracker to study central heavy ion collisions with up to several thousand particles in an event, at more than 100 events per second.

The basic design elements have hardly changed over the years. Cylindrical field cages provide a homogeneous electric field between the central electrode and the planar wire chambers at both ends; see Fig. 4.25 for the conceptual design of the latest TPC in operation, the STAR TPC at RHIC [64]. The typical gas mixture is Ar/CH_4, which offers high drift velocity at low electric field and low electron attachment. The electrons from the track ionization drift to one of the two endcaps. They traverse a gating grid and a cathode grid before being amplified on 20 μm anode wires, separated with field wires. The avalanche position along the wires is obtained from measuring the centre of gravity of pulse heights from pads of the segmented cathode beneath. Figure 4.26 shows the electric field lines for a closed and an open gating grid. *Gating* is essential for the TPCs with their long drift length, to reduce space charge build-up. The gate is only opened on a trigger.

All TPCs except PEP4 and TOPAZ operated at latm and profit from a strong reduction of lateral diffusion due to the factor $\omega\tau$~5 in the strong magnetic field B oriented parallel to the electric field E. Higher pressure is rather neutral: $\omega\tau$ decreases, but more primary electrons reduce relative fluctuations and thus **ExB** and track angle effects. Typical point resolutions in $r\Phi$ range from 150 to 200 μm at the e^+e^- colliders [65]. Figure 4.27 shows a reconstructed Pb–Pb interaction observed in STAR.

All TPCs except STAR and ALICE use the signals from the anode wires for dE/dx information. In STAR and ALICE, all information is taken from the pads, some 560,000 in ALICE [14]. Pressure improves dE/dx and the PEP4 TPC operating at 8.5 atm produced the best dE/dx resolution despite a smaller radius [65].

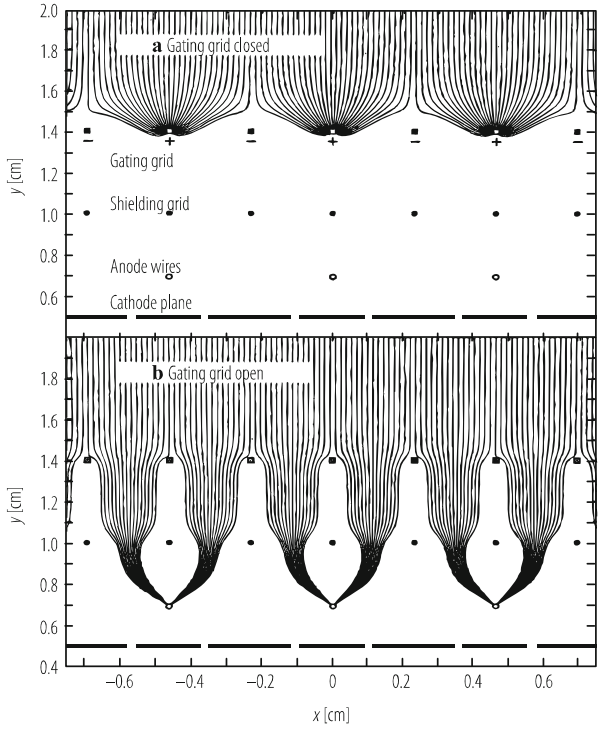

Fig. 4.26 TPC wire chamber: electric field lines for a closed (**a**) and open *x* [cm] gating grid **(b)**

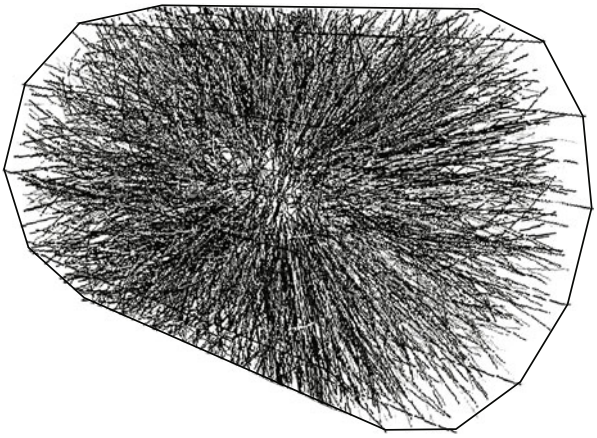

Fig. 4.27 A reconstructed Pb–Pb interaction observed in the STAR TPC [64]

4.3.4 Parallel Plate Geometries, Resistive Plate Chambers (RPCs)

Parallel plate devices offer fast response, as there is no drift delay and the avalanche amplification starts immediately.

Keuffel's spark counter [6] featured two metal electrodes at millimeter distance in a gaseous atmosphere, where the primary electrons deposited in the gap provoke a fast discharge and therefore a detectable signal. By the end of the 1960s the spark counters had arrived at time resolutions around 100 ps, the rates however were limited to 1 kHz and small areas of about 30 cm^2, since after each discharge the entire counter was insensitive during the recharge time of typically a few hundred microseconds. Parallel Plate Chambers (PPCs) use the same geometry but operate below the discharge voltage. The avalanche therefore induces a signal but does not create a discharge, allowing a rate capability of 100 kHz for a 80 cm^2 detector [6]. Still, the fact that the detector mechanics and especially the detector boundaries have very carefully controlled to ensure stability, limits this detector to a rather small surface.

The Pestov spark counter [66] uses the same parallel plate geometry, with one electrode made from resistive material having a volume resistivity of $\rho = 10^9 - 10^{10}$ Ωcm. The charge deposited locally on this resistive layer takes a time of $\tau \approx \rho\varepsilon$ to be removed, where ε is the permittivity of the resistive plate. This time is very long compared to the timescale of the avalanche process, the electric field is therefore reduced at the location of the avalanche, avoiding a discharge of the entire counter. This allows stable operation of the detector at very high fields and particle rates. A counter with a size of 600 cm^2 and a gas gap of 1 mm, operated at atmospheric pressure achieved a time resolution of <0.5 ns and efficiency of 98%. By decreasing the size of the gas gap to 0.1 mm and operating the detector at 12 bar pressure, a time resolution of 27 ps was achieved with this detector [67].

Resistive Plate Chambers (RPCs) [68] are building on this same principle and they are widely used as trigger detectors and for time-of-flight measurements, as they allow relatively cheap large area construction. Large detector systems of several hundred m^2 surface have been built with Bakelite plates ($\rho = 10^{10} - 10^{12}$ Ωcm) or window glass ($\rho = 10^{12} - 10^{13}\,\Omega$ cm). Tetrafluorethane ($C_2F_4H_2$) is nowadays widely used as the main component of the RPC gas mixture due to the large number of primary ionization clusters (8–10/mm) leading to large detection efficiency and due to it's electronegativity that reduces the probability for the formation of streamers. Small additions of SF_6 are further reducing this streamer probability.

The time resolution for RPCs is given by $\sigma_t \approx 1.28/\alpha v$, where α is the effective Townsend coefficient of the gas mixture and v is the drift-velocity of the electrons. RPCs with a single gas gap of 2 mm at a field of 50 kV/cm ($\alpha \approx 10$/mm, $v \approx 130\,\mu$m/ns) provide a time resolution of ≈1 ns and efficiency close to 100%. Figure 4.28a shows the geometry as used for the muon system of the ATLAS experiment. In addition to collider experiments, similar geometries are used as

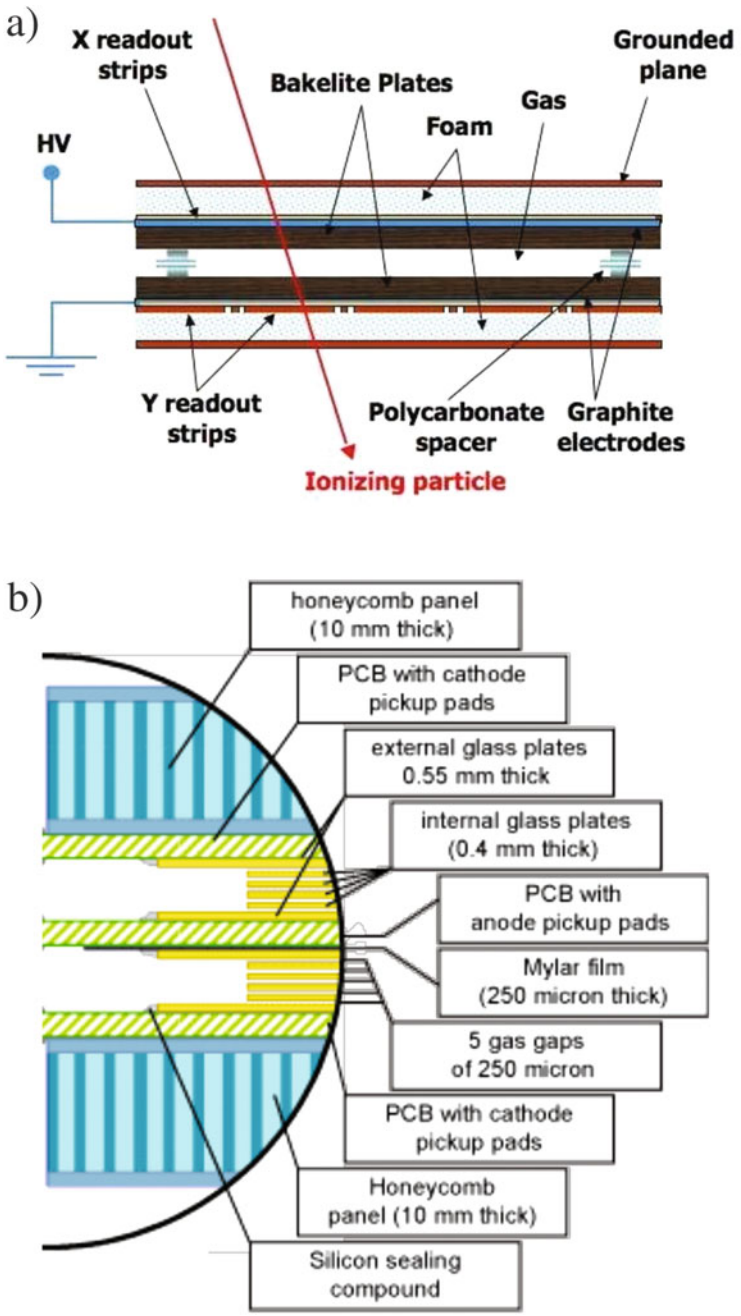

Fig. 4.28 (**a**) Single gap RPC as used by the ATLAS experiment for the muon trigger system. (**b**) Multigap RPC as used by the ALICE experiment for the time of flight system

trigger or veto detectors in neutrino experiments like OPERA [69] and Daya Bay [70] and as large area cosmic ray detectors like ARGO [71].

Using a small gas gap of 0.25–0.3 mm with a field around 100 kV/cm ($\alpha \approx 113$/mm, $v \approx 210\,\mu$m/ns) results in a time resolution of $\approx$50 ps, making the detector well suited for time-of-flight measurements. The reduced efficiency due to the narrow gas gap is overcome by using a multi-gap structure [83]. Figure 4.28b shows the geometry as used for the time of flight system of the ALICE experiment. The avalanche process in RPCs is significantly affected by spacecharge effects. After the initial exponential increase of the electron number, the ions produced in the avalanche are significantly reducing the electric field and therefore resulting in strong slow down of the avalanche growth. This results in moderate signal charges in the pC range even for very large Townsend coefficients [72].

The rate capability of RPCs is defined by the thickness d of the resistive plates and their volume resistivity ρ. The current I produced per unit area inside the gas gap is flowing through these plates, which results in an effective voltage drop of $\Delta V = I\rho d$ across a single plate. The rate limit of the RPC is reached at the point where the effective voltage across the gas gap moves outside the efficiency plateau. For the values and geometries quoted above, this limit is in the range of 10–1000 Hz/cm^2.

4.3.5 Micropattern Devices

The constantly increasing particle rates and track densities in modern day experiments exceed the capabilities of standard gaseous detectors. Semiconductor technology dominates this regime. On the other hand, numerous novel designs of gaseous detectors have been studied. Two have emerged and attract much attention, the so-called GEM and Micromegas devices. Offering small ExB track distortions and low ion feedback, they are also being used for the readout of TPCs.

4.3.6 Gas Electron Multiplier (GEM)

In a thin metal-coated polymer foil, holes are chemically etched at high special density [73], see Fig. 4.29. A voltage applied to the metal layers produces gas amplification in the holes. Typical parameters are: Foil thickness = 50 μm, inner hole diameter = 70 μm, hole pitch = 140 μm, voltage = 400 V. To achieve a practical gas gain of the order of $10^4 - 10^5$ with an acceptable low discharge probability, usually three GEMs are put in series. In COMPASS [74], a system of 20 triple-GEMs with an active area of 31 $\times$ 31 cm^2 each was operated in a very high intensity muon beam. With 2-D readout via superposed orthogonal strips, a space resolution of 70 μm was achieved at rates up to 2.5 MHz/cm^2. The efficiency was 99% with 50 ns pulse shaping at an effective gain of 8000.

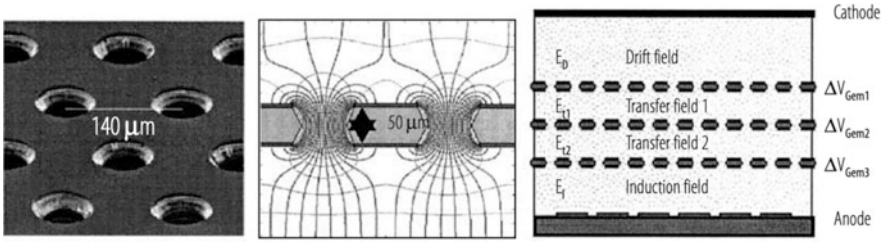

Fig. 4.29 GEM. Left: hole structure. Centre: electric field lines. Right: Conceptual design of tripleGEM [73]

In LHCb [75], with a much shorter peaking time of 10 ns, an efficiency of $\geq$96% was reached for two triple-GEMs in OR and a gain of 6000 with $Ar/CO_2/CF_4$ (45/15/40). The time resolution with this chamber was $\leq$3 ns with Ar/CO_2 (70/30).

Charge build-up is observed on the insulating holes in the GEM foils, which varies with the particle flux and is accompanied by some change in gain, well described by simulation [76].

Several large scale GEM systems are under construction. The wire chambers of the ALICE TPC are replaced by an a quadruple-GEM arrangement that is optimized for low ion backflow. This allows the TPC to operate in continuous mode without the need for gating. The top and bottom GEMs have a hole separation of 140 μm as described above, while the two middle GEMs have twice this distance. This results in an ion feedback below 1% and energy resolution of <12% for 5.9 keV photons at an effective gain of $\approx$2000 [77].

The muon system of the CMS experiment is being equipped with standard triple-GEM detectors over a surface of $\approx$220 m^2 providing spatial resolution of $200 - 400\,\mu$m and a time resolution of 8 ns [78].

4.3.7 Micromegas

In a Micromegas detector [79], the ionization produced in the drift gap is channeled through an extremely fine mesh into the amplification gap, terminated by an anode plane segmented into readout strips or pads as seen in Fig. 4.30. The 'micromesh' is woven from $\approx 15\,\mu$m wires leaving holes of about 50 μm^2. The amplification gap is only 50–150 μm thick and behaves on average like a parallel counter. The mesh is supported by pillars every $\approx$2.5 mm. Due to the high amplification field in comparison to the drift field, the electrons are moving to the anode only inside a very thin funnel, see Fig. 4.30.

In the COMPASS experiment, 12 chambers 40×40 cm^2 have operated in fluxes up to 25 MHz/mm^2 and obtained resolutions of 70–90 μm and 9 ns. The near detector of the T2K experiment [75] uses a TPC with 9 m^2 of MICROMEGAs detectors with readout pads of 10×7 mm^2. The muon system of the ATLAS detector is

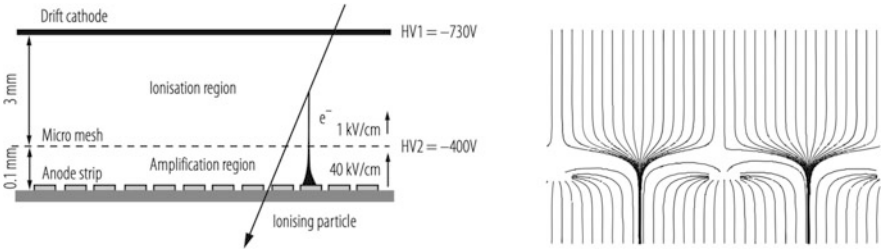

Fig. 4.30 Micromegas. Left: conceptual design. Right: Electrical field lines

implementing two 'wheels' of 8 m diameter with 4 layers of MICROMEGAs [80]. The readout readout strips of 300 μm width achieve a position resolution around 100 μm. In order to increase the stability against discharges for these very large surfaces, resistive strips are placed on top of the readout strips at a distance of 64 μm. The resistance value of 10–20 MΩ/cm ensures that the rate capability is sufficient for the application.

4.4 Outlook

The availability of large area silicon sensors has allowed most of the recent detector setups to use silicon trackers for vertexing and momentum spectroscopy in the detector volume upstream of the calorimeter systems. Muon systems do however have surfaces of up to several thousands of m^2 with particle rates and resolution requirements that make the application of gas detectors still the most viable solution. The TPC is still a very appealing detector for setups where very low material budget as well as PID capabilities are important requirements. Experiments such as NEXT [81] for the search of neutrinoless double beta decay are building on the unique features of gas detectors like low density of the detection medium and the related possibility for tracking of very low energy particles. Gas detector will therefore continue to be essential elements of particle physics instrumentation.

The last two sections on Resistive Plate Chambers and Micropattern Devices were updated in this new edition, while the remainder of this chapter is in its original form by H.J. Hilke.

References

1. E. Rutherford, H. Geiger, Proc. Roy. Soc. London A 81 (1908) 141.
2. H. Geiger, Verh. D. Phys. Ges. 15 (1913) 534.
3. H. Greinacher, Z. Phys. 23 (1924) 261.
4. H. Geiger, W. Mueller, Phys. Z. 29 (1928) 839.

5. A. Trost, Z. Phys. 105 (1937) 399.
6. (a) J.W. Keuffel, Rev. Sci. Instrum. 20 (1949) 202; (b) J. Christiansen, Z. Angew. Phys. 4 (1952) 326.
7. E. Fuenfer, H. Neuert, Zählrohre und Szintillationszähler, G. Braun, Karlsruhe (1959).
8. G. Charpak et al., *The Use of Multiwire Proportional Counters to select and localize Charged Particles*, Nucl. Instrum. Meth. 62 (1968) 262.
9. T. Bressani, G. Charpak, D. Rahm, C. Zupancic, *Track Localization by Means of a Drift Chamber*, Proc. Int. Seminar Filmless Spark and Streamer Chambers, Dubna, USSR, 1969, p. 275.
10. A.H. Walenta, J. Heintze and B. Schürlein, *The Multiwire Drift Chamber-A Novel Type of Proportional Wire Chamber*, Nucl. Instrum. Meth. 92 (1971) 373.
11. R. Veenhof, *Garfield-simulation of gaseous detectors*, http://consult.cem.ch/writeup/garfield/
12. I. Smimov, *Heed*: *Interactions ofparticles with gases*, http://consult.cem.ch/writeup/heed/
13. S. Biagi, *Magboltz*: *Transport of electrons in gas mixtures*, http://consult.cem.ch/writeup/magboltz/
14. The ALICE experiment at the CERN LHC, J. Instrum. 3 (2008) S08001.
15. The ATLAS Experiment at the CERN LHC, J. Instrum. 3 (2008) S08002.
16. The CMS experiment at the CERN LHC, J. Instrum. 3 (2008) S08003.
17. The LHCb Detector at the LHC, J. Instmm. 3 (2008) S08004.
18. Special volumes of Nucl. Instrum. Methods: the last three Proceedings are found in Nucl. Instrum. Meth. A 581 (2007) 1; 535 (2004) 1; 478 (2002) 1.
19. W. Blum, W. Riegler, L. Rolandi, Particle Detection with Drift Chambers, 2nd ed., Springer-Verlag (2008).
20. H. Bichsel, (a) Nucl. Instrum. Meth. A 562 (2006) 154; (b) Phys. Lett. B667 (2008) 267.
21. Review Particle Physics, Phys. Lett. B667(1–5) (2008) 292.
22. F. Lapique, F. Piuz, Nucl. Instrum. Methods 175 (1980) 297
23. H. Fischle, J. Heintze, B. Schmidt, Nucl. Instrum. Methods 301 (1991) 202
24. H. Walenta, Nucl. Instrum. Methods 161 (1979) 45.
25. I. Lehraus et al., Nucl. Instrum. Methods 153 (1978) 347
26. J. Va'vra et al. SLAC-PUB-5728, (1992).
27. S.F. Biagi, Nucl. Instrum. Meth. A 283 (1989) 716; ref. to J.C. Armitage, Nucl. Instrum. Meth. A 271 (1988) 588.
28. B. Schmidt, Doctoral thesis, Univ. Heidelberg, (1986).
29. G. Schultz, Doctoral thesis, Univ. Louis-Pasteur, Strasbourg, (1979).
30. Review Particle Physics, Physics Letters. B667(1–5) (2008) 1.
31. Compilation by A. Jeavons et al., Nucl. Instrum. Meth. 176 (1980) 89–97.
32. J.H. Hombeck, Phys. Rev. 84 (1951) 615.
33. (a) RD-32, CERN/DRDC 94-10 (1994); (b) A. Ishikawa, http://www-hep.phys.saga-u.ac.jp/ILC-TPC/gas/ps/
34. E.B. Wagner, F.J. Davies, F.J. Hurst, J. Chem. Phys. 47 (1967) 3138.
35. J.H. Parker, J.J. Lowke, Phys. Rev. 181 (1969) 290 and 302
36. PEP-4 Proposal, SLAC-Pub-5012 (1976).
37. S.R. Amendolia et al., Nucl. Instrum. Meth. 244 (1986) 516.
38. H.S.W. Massey, E.H.S. Burhop, H.B. Gilbody, Electronic and ionic impact Phenomena, Clarendon, Oxford (1969).
39. D.L. McCorkle, L.G. Christophorou, S.R. Hunter, in: Proc. 2nd Int. Swarm Seminar, Oak Ridge, USA, Pergamon, New York (1981) p. 21.
40. F. Bloch, N.E. Bradbury, Phys. Rev. 48 (1935) 689.
41. M. Atac, A.V. Tollestrup, D. Potter, Nucl. Instrum. Meth. 200 (1982) 345.
42. Collected by A. von Engel, Handbuch der Physik 21 (1956), Springer, Berlin.
43. M.E. Rose, S.A. Korff, Phys. Rev. 59 (1941) 850.
44. W. Diethom, USAEC Report NY 6628 (1956).
45. G.A. Erskine, Nucl. Instrum. Meth. 105 (1972) 565.
46. C. Brand et al. Nucl. Instrum. Meth. A 237 (1985) 501.

47. W. Legler, Z. Naturforschung A 16 (1961) 253.
48. H. Schlumbohm, Z. Phys. 151 (1958) 563.
49. G.D. Alkahazov, Nucl. Instrum. Meth. 89 (1970) 155.
50. S.C. Curran, A.L. Cockroft, J. Angus, Philos. Mag. 40(1949) 929.
51. S. Ramo, Proc. I.R.E. 27(1939) 584.
52. W. Shockley, J. Appl. Phys. 9 (1938) 635.
53. OPAL Collaboration, *The OPAL Detector at LEP*, Nucl. Instrum. Meth. A 305 (1991) 275.
54. (a) Proc. Workshop Radiation Damage to Wire Chambers, Berkeley (org. J. Kadyk), LBL 21170 (1986); (b) Proc. Int. Workshop Aging Phenomena in Gaseous Detectors, Hamburg, 2001, Nucl. Instrum. Meth. A 515 (2003); (c) NASA, a very large database on outgassing of materials can be reached via the NASA home- page.
55. (a) J. Va'vra, Nucl. Instrum. Meth. A 515 (2003) 263, and N. Tesch, IEEE Trans. Nucl. Sci. 49 (2002) 1609; (b) M. Capeans, Nucl. Instrum. Meth. A 515 (2003) 73; (c) R. Bouclier et al., Nucl. Instrum. Meth. A 350 (1994) 464.
56. J. Adam et al., Nucl. Instrum. Meth. 217 (1983) 291.
57. L. Malter, Phys. Rev. 50 (1936) 48.
58. C. Bemporad, Nucl. Instrum. Meth. 80 (1969) 205.
59. P. Schilly et al., Nucl. Instrum. Meth. 91 (1970) 221.
60. G. Charpak, D. Rahm, H. Steiner, Nucl. Instrum. Meth. 80 (1970) 13.
61. R. Bouclier et al., Nucl. Instrum. Meth. 115 (1973) 235
62. D.R. Nygren, Proposal to investigate a novel concept in particle detection, LBL intemal report, Berkeley, February 1974.
63. Proposal for a PEP Facility based on the Time Projection Chamber, PEP 4, Dec. 1976.
64. M. Anderson et al., *The STAR Time Projection Chamber*, Nucl. Instrum. Meth. A 499 (2003) 659.
65. (a) A. Shirahashi et al., *TOPAZ Time Projection Chamber*, IEEE Trans. NS-55 (1988) 414; (b) W.B. Atwood et al., *ALEPH Time Projection Chamber*, Nucl. Instrum. Meth. A 306 (1991) 446; (c) P. Abreu et al., *DELPHI Detector*, Nucl. Instrum. Meth. A 178 (1996) 57; (d) J. Alme et al., *The ALICE TPC*, Nucl. Instrum. Meth. A 622 (2010) 316-367; (e) a review on TPCs: H.J. Hilke, Rep. Prog. Phys. 73 (2010) 116201.
66. V.V. Parkhomchuk, Y.N. Pestov and N.V. Petrovykh, A spark counter with large area, Nucl. Instr. and Meth. A 93 (1971) 269–270.
67. Yu.N. Pestov, Status and future developments of spark counters with localized discharge, Nucl. Instr. and Meth. A 196 (1982) 45–47.
68. R. Santonico, R. Cardarelli, Development of Resistive Plate Counters, Nucl. Instr. and Meth. A 187 (1981) 377.
69. A. Bertolin et al., The RPC system of the OPERA experiment, Nucl. Instr. and Meth. A 602 (2009) 631–634.
70. J. Cao and Kam-Biu Luk, An overview of the Daya Nay reactor neutrino experiment, Nuclear Physics B 908 (2016) 62–73.
71. G. Aielli et al., Layout and performance of the RPCs used in the Argo-YBJ experiment, Nucl. Instr. and Meth. A 562 (2006) 92–96.
72. W. Riegler et al., Detector physics and simulation of Resistive Plate Chambers, NIMA 500 (2003) 144–162.
73. F. Sauli, Nucl. Instrum. Meth. A 386 (1997) 531.
74. B. Ketzer et al., Nucl. Instrum. Meth. A 535 (2004) 314.
75. N. Abgrall et al., Time projection chambers for the T2K near detectors, NIMA 637 (2011) 25–46.
76. V. Tikhonov, R. Veenhof, Nucl. Instrum. Meth. A 478 (2002) 452.
77. M.M. Aggarwal et al. NIM A 903 (2018) 215.
78. D. Abbaneo et al., Upgrade of the CMS muon system with tripple-GEM detectors, JINST 9 C10036.
79. Y. Giomataris, Nucl. Instrum. Meth. A 419 (1998) 239.

80. F. Kuger et al., Performance studies of the resistive Micromegas detectors for the upgrade of the ATLAS Muon spectrometer, NIMA 845 (2017) 248–252.
81. J.J. Gomez-Cadenas, The next experiment, NPPP 273-275 (2016) 1732–1739.
82. IAEA-TECDOC-799 (1995) 560, Atomic and Molecular Data for Radiotherapy.
83. A. Akindinov et al., The multigap resistive plate chamber as a time-of-flight detector, Nucl. Instr. and Meth. A 456 (2000) 16.